MNRAS 000, 1–18 (2024) Preprint 26 June 2025 Compiled using MNRAS LATEX style file v3.0

arXiv:2506.20301v1 [astro-ph.EP] 25 Jun 2025

Can tidal evolution lead to close-in planetary bodies around white dwarfs I: Orbital period distribution

Yuqi Li,[1★] Amy Bonsor,[1] Oliver Shorttle,[1,2] and Laura K. Rogers[1]
[1]Institute of Astronomy, University of Cambridge, Madingley Road, Cambridge, CB3 0HA, UK
[2]Department of Earth Sciences, University of Cambridge, Downing Street, Cambridge, CB2 3EQ, UK

Accepted XXX. Received YYY; in original form ZZZ

ABSTRACT

The evolution of planetary systems around white dwarfs is crucial to understanding the presence of planetary material in the atmospheres of white dwarfs. These systems uniquely probe exoplanetary compositions. Periodic signals in the photometry of a handful of white dwarfs suggest material blocking the star, potentially from disintegrating planetesimals. Tidal evolution followed by scattering can bring planetesimals onto close-in orbits that would have been within the envelope of the white dwarf progenitor. The orbital period distribution of planetesimals undergoing tidal evolution will peak at short-period (nearly) circularized orbits ($\sim$ 10 hour–1 day), with a rising tail towards long-period highly eccentric orbits ($\sim$ 100 day). This prediction is generally consistent with the observed white dwarf transiting systems. In order for the planetesimal on the 4.5 hour period around WD 1145+017 to be explained by the tidal evolution of a planetesimal, that planetesimal must have an ultimate tensile strength comparable to that of iron meteorites.

Key words: white dwarfs – planets and satellites: general – planets and satellites: dynamical evolution and stability – planet–star interactions

1 INTRODUCTION

White dwarfs that have recently accreted planetary material provide a unique tool to probe the composition of planetary bodies outside the solar system. White dwarfs are the left-over degenerate cores of low to intermediate mass stars. The high surface gravity of white dwarfs leads to rapid gravitational settling of metals (elements heavier than helium). However, observations reveal that $\sim$ 10%–50% of the white dwarfs are contaminated with metals, suggesting recent/ongoing accretion of the remaining planetary bodies around the white dwarfs (Zuckerman et al. 2003, 2010; Koester et al. 2014; Wilson et al. 2019; O'Brien et al. 2023, 2024; Manser et al. 2024).

The mechanism that leads to the accretion of planetary material onto white dwarfs remains unclear. The widely accepted theory is that planetesimals (planetary building blocks) are gravitationally scattered towards the white dwarf under the effect of massive perturbers, for instance, planets (Bonsor et al. 2012; Mustill et al. 2018; Rodet & Lai 2024). These scattered planetesimals end up entering the white dwarf atmosphere. The accretion onto white dwarfs can be observed in action, with both dusty material (infrared excess) and gas (circumstellar absorption/emission features) detected (Zuckerman & Becklin 1987; Becklin et al. 2005; Kilic et al. 2005, 2006; Gänsicke et al. 2007; Jura et al. 2007; Farihi et al. 2009; Jura et al. 2009; Farihi et al. 2010; Melis et al. 2010; Debes et al. 2012; Xu et al. 2015; Bonsor et al. 2017; Xu et al. 2020; Lai et al. 2021; Wang et al. 2023) (see Farihi 2016 for a detailed review).

Further observational evidence for accretion in action comes from the first identification of transits around a polluted white dwarf with an infrared excess, WD 1145+017 using the Kepler K2 data (Vanderburg et al. 2015). Follow-up observations from 2015–2017 reconfirm the dominant period in K2 data, the 4.5 hr period ('A' period), with variable weaker periodic signals (Vanderburg et al. 2015; Gänsicke et al. 2016; Rappaport et al. 2016; Croll et al. 2017; Gary et al. 2017).

There is a rich literature that attempts to explain the origin of the transiting features of WD 1145+017. One popular model motivated by the longer egress time and unexpectedly long transit duration consistent with the light curves of disintegrating planets around main sequence stars (Kawahara et al. 2013; van Lieshout et al. 2014; Rappaport et al. 2014; Sanchis-Ojeda et al. 2015; van Lieshout et al. 2016) is a planetesimal with active dust/gas production orbiting the white dwarf with a period of 4.5 hr (Rappaport et al. 2016; Veras et al. 2017; Duvvuri et al. 2020; O'Connor & Lai 2020).

The second identified transiting white dwarf system, ZTF J0139+5245, possesses a much longer period (107.2 day) than WD 1145+017 (Vanderbosch et al. 2020). 5 more potential white dwarf transiting systems are identified (Guidry et al. 2021), among which ZTF J0328-1219 with robust evidence of transits is further studied and two transiting periods 9.937 hr and 11.2 hr are found (Vanderbosch et al. 2021). Meanwhile, another system with transits, WD 1054-226 (period 25.02 hr) is reported (Farihi et al. 2022). With the increase in publicly available light curves from past and present facilities such as: Kepler/K2 (Borucki et al. 2010; Howell et al. 2014), the Transiting Exoplanet Survey Satellite (*TESS*, Ricker et al. 2014), *Gaia* (Gaia Collaboration et al. 2016), and the Zwicky Transient Facility (ZTF, Bellm et al. 2019), and future facilities such as: the Large Synoptic Survey Telescope (LSST, Ivezić et al. 2019), more transit candidates should be identified, with extensive high-speed photo-

---

★ E-mail: yl817@cam.ac.uk

© 2024 The Authors

metric follow-ups usually required to confirm the transits and obtain the transit periods (e.g., Guidry et al. 2021; Vanderbosch et al. 2021; Farihi et al. 2022).

The transiting systems provide clear observational evidence for planetary material close to the white dwarfs, potentially undergoing active dust/gas production. If the planetary material has not undergone a common envelope event, orbital decay/circularization after gravitational scattering may be required to bring planetary material close to the white dwarfs, with tidal evolution a potential mechanism (Veras & Fuller 2019, 2020; O'Connor & Lai 2020).

In the solar system, the tidal effect is responsible for the spin-down of the Earth accompanied with the outward migration of the moon, which help constrain the origin and the evolution history of the Earth-moon system (Goldreich 1966; Kagan 1997; Neron de Surgy & Laskar 1997; Zahnle et al. 2015; Tyler 2021; Farhat et al. 2022; Downey et al. 2023). Tidal interactions also give rise to the solar system's volcanically active moon, Io (Tyler et al. 2015; Rathbun et al. 2018; Kervazo et al. 2022; Davies et al. 2024; Seligman et al. 2024). Meanwhile, tidal theory has also been applied to bodies outside the solar system, for instance, eccentric migration potentially responsible for the formation of hot (and sometimes inflated) Jupiters (Miller et al. 2009; Ibgui et al. 2010; Leconte et al. 2010; Dong et al. 2021; Rozner et al. 2022; Glanz et al. 2022; Vick et al. 2023). Veras et al. 2019 investigated the parameter space where tidal evolution brings planets into the Roche limit of white dwarfs. Veras & Fuller 2019, 2020 and O'Connor & Lai 2020 incorporated tidal evolution to explain the (potential) presence of close-in planetary bodies around white dwarfs and constrain the tidal-related parameters of the bodies based on their current orbits and the cooling ages of the white dwarfs.

In this paper, following the idea that tidal evolution may lead to close-in planetary bodies around white dwarfs, we examine the scenario that a population of surviving planetesimals scattered onto highly eccentric orbits external to, and close to the Roche limit of the white dwarfs tidally evolve onto various shorter-period orbits. By tracing the orbital parameters of scattered planetesimals undergoing tidal evolution, we:

- investigate the parameter dependence of tidal circularization timescale,
- predict the distribution of orbital periods shaped by tidal evolution at a given epoch,
- compare the predicted orbital period distribution to periodic signals seen for white dwarfs with transit features
- constrain the physical properties of the transiting planetesimals and compare to Solar System asteroids.

The paper starts by summarising the model used to follow the tidal evolution of scattered planetesimals (Section 2) and predict the resultant orbital period distribution. The tidal evolution of an individual planetesimal of given properties is presented in Section 3.1, highlighting the key factors affecting the tidal circularization timescale (Section 3.1.2). By considering the probability of scattering planetesimals to different initial pericentres, the probability distribution of the orbital periods is calculated in Section 3.2. Then, we discuss the limitations in the tidal model (Section 4.1) and the uncertainties in the population of planetesimals scattered close to the white dwarf (Section 4.2), together with the corresponding effects on the orbital period distribution. In Section 4.4, we present a synthetic orbital period distribution accounting for a population of planetesimals with a range of properties scattered at different times and compare to current observations. Finally, we discuss the implications of the model in Section 4.5 and in Section 5, we summarize our results.

2 METHODS

Towards the end of the asymptotic giant branch/start of the white dwarf phase, the host star loses a substantial amount of its mass, weakening its gravitational attraction. As a result, the planetary system tends to become less stable against gravitational perturbations (Bonsor et al. 2011; Veras 2016; O'Connor et al. 2022). Under the growing gravitational effects of perturbers (e.g., planets), the orbital parameters of planetary bodies are altered (via, e.g., scattering), leading to phenomena such as ejection and tidal disruption, with the latter a plausible pathway of polluting the photosphere of the white dwarf (Mustill et al. 2018; Veras et al. 2021, 2023; Rodet & Lai 2024; Veras et al. 2024). In this paper, we will use the term scattering to refer to the delivery of planetesimals close to the white dwarf, but we acknowledge the existence of other mechanisms (e.g., secular chaos O'Connor et al. 2022, mean motion resonances Veras et al. 2023).

The method presented in this work utilises the constant time lag (CTL) model of tidal evolution to predict the orbital evolution of planetesimals scattered close to the white dwarf after leaving the instability zone (which we define as $t = 0$). The aim is to predict the orbital period distribution of planetesimals after a certain time of tidal evolution, based on an assumption for the scattering process.

In this section, we:

- summarizing the CTL model (Section 2.1), outlining the coupled evolution equations (Section 2.1.1) and listing the key properties of the model (Section 2.1.2),
- derive the Roche limit accounting for the ultimate tensile strength of the planetesimal and pseudo-synchronous spin predicted by the constant time lag model, which constrains the orbital parameter space where a planetesimal avoids tidal disruption (Section 2.2),
- summarize the method and list the choice of free parameters (Section 2.3).

2.1 The constant time lag model

In this study, we use the CTL model to predict the orbital evolution of planetesimals scattered close to the white dwarf, external to the Roche limit (Section 2.2), after the planetesimals leave the instability zone (where scattering occurs). Under the CTL model, the tidal force exerted by the white dwarf raises tidal bulges on the planetesimal that lag behind the equipotential surface for a constant time interval Δt, inducing angular momentum transfer and dissipation of orbital energy (Hut 1981; Levrard et al. 2007; Leconte et al. 2010; Matsumura et al. 2010; Bolmont et al. 2011; Heller et al. 2011; Beaugé & Nesvorný 2012; Hansen 2012; Glanz et al. 2022; Rozner et al. 2022; Lu et al. 2023). Although more realistic models exist, the unconstrained properties of exoplanetary bodies and the complex coupling between rheological and tidal evolution also add more uncertainties (Section 4.1).

2.1.1 *Evolution equations*

The coupled tidal evolution equations for a white dwarf-planetesimal (two-body) system, expanded to the lowest order in Δt and to the fifth order in $\frac{R}{r}$ are of the form (Hut 1981; Levrard et al. 2007; Leconte et al. 2010; Matsumura et al. 2010; Bolmont et al. 2011; Heller et al. 2011; Beaugé & Nesvorný 2012; Hansen 2012; Glanz et al. 2022; Rozner et al. 2022; Lu et al. 2023) (with the symbols defined in Table 1):

Subscripts	
p	planetesimal
$*$	white dwarf
0	$t = 0$, the point of leaving the scattering zone
	orbital evolution dominated by tide
eq	equilibrium state under the CTL model
Constants	
G	gravitational constant
$M_\odot$	solar mass
Constant parameters	
M	mass
R	radius
ρ	bulk density
k_2	potential love number of degree 2
Δt	constant time lag
K	$K \equiv 3k_2\Delta t$
I	moment of inertia
σ_s	ultimate tensile strength
C	$C \equiv \frac{I}{MR^2}$
T_p	$T_p \equiv \frac{K_p(M_p+M_*)M_*R_p^5}{M_p} \approx \frac{K_pM_*^2R_p^5}{M_p}$
Orbital parameters	
e	eccentricity
a	semi-major axis
T	orbital period
q	pericentre distance
	$q = a(1-e)$
Q	apocentre distance
	$Q = a(1+e)$
ω	spin
	$\mathrm{sgn}(\omega) = \mathrm{sgn}(\cos\epsilon)$
ϵ	obliquity
r_{Roche}	Roche limit
n	mean motion
	$n = \sqrt{\frac{G(M_p+M_*)}{a^3}}$
η	ratio of spin to orbital angular momentum
	$\eta \equiv C\frac{M_p+M_*}{M_pM_*}M\frac{R^2}{a^2}(1-e^2)^{-\frac{1}{2}}\frac{\omega}{n}$
Time	
t	tidal evolution time
$t = 0$	the time of leaving the scattering zone
τ_{cir}	Tidal circularization timescale

Table 1. Definitions of the symbols used in this paper.

$$\frac{de}{dt} = \sum_{i=p,*} 9K_i n \frac{M_pM_*}{M_i^2}\frac{R_i^5}{a^5}e(1-e^2)^{-\frac{13}{2}} \times \left[\frac{11}{18}(1-e^2)^{\frac{3}{2}}f_4(e)\omega_i\cos\epsilon_i - f_3(e)n\right], \tag{1}$$

$$\frac{da}{dt} = \sum_{i=p,*} 2K_i n \frac{M_pM_*}{M_i^2}\frac{R_i^5}{a^4}(1-e^2)^{-\frac{15}{2}} \times \left[(1-e^2)^{\frac{3}{2}}f_2(e)\omega_i\cos\epsilon_i - f_1(e)n\right], \tag{2}$$

$$\frac{d\omega_i}{dt} = K_i n^2 \frac{(M_pM_*)^2}{(M_p+M_*)M_i^3}\frac{R_i^3}{a^3}\frac{1}{C_i}(1-e^2)^{-6} \times \left[f_2(e)n\cos\epsilon_i - \frac{1}{2}(1+\cos^2\epsilon_i)(1-e^2)^{\frac{3}{2}}f_5(e)\omega_i\right], \tag{3}$$

$$\frac{d\epsilon_i}{dt} = K_i n^2 \frac{(M_pM_*)^2}{(M_p+M_*)M_i^3}\frac{R_i^3}{a^3}\frac{\sin\epsilon_i}{\omega_iC_i}(1-e^2)^{-6} \times \left[\frac{1}{2}(\cos\epsilon_i - \eta_i)(1-e^2)^{\frac{3}{2}}f_5(e)\omega_i - f_2(e)n\right], \tag{4}$$

where the subscript i represents the contribution of the tide induced on the object i by the other object to the evolution of the system, and f_1 to f_5 are of the form:

$$\begin{aligned}
f_1(e) &= 1 + \frac{31}{2}e^2 + \frac{255}{8}e^4 + \frac{185}{16}e^6 + \frac{25}{64}e^8,\\
f_2(e) &= 1 + \frac{15}{2}e^2 + \frac{45}{8}e^4 + \frac{5}{16}e^6,\\
f_3(e) &= 1 + \frac{15}{4}e^2 + \frac{15}{8}e^4 + \frac{5}{64}e^6,\\
f_4(e) &= 1 + \frac{3}{2}e^2 + \frac{1}{8}e^4\\
f_5(e) &= 1 + 3e^2 + \frac{3}{8}e^4.
\end{aligned} \tag{5}$$

For a planetesimal-white dwarf system considered in this work, we focus on the tide raised on the planetesimal by the white dwarf (planetesimal tide, $i = p$ terms) because the contributions of white dwarf tide is negligible: the ratio of the contributions of $i = p$ terms to that of $i = *$ terms can be approximated as $\frac{K_p}{K_*}\frac{\rho_*^2R_*}{\rho_p^2R_p} \sim \frac{K_p}{K_*}10^{11}$ with $\log_{10}\frac{K_p}{K_*} \sim 10$ (Willems et al. 2010; Veras & Fuller 2019; Becker et al. 2023).

2.1.2 *Properties of the model*

The key properties of the CTL model (Hut 1981; Levrard et al. 2007; Leconte et al. 2010; Matsumura et al. 2010; Bolmont et al. 2011; Heller et al. 2011; Beaugé & Nesvorný 2012; Hansen 2012; Glanz et al. 2022; Rozner et al. 2022; Lu et al. 2023) for a white dwarf-planetesimal system are summarized below (see appendices A, B, and see Table 2 for a summary):

- The orbital angular momentum of the white dwarf-planetesimal system is conserved during tidal evolution, such that semi-major axis and eccentricity evolution is constrained by the initial pericentre distance (q_0) and apocentre distance (Q_0) via:

$$a(1-e^2) = \frac{2q_0Q_0}{q_0+Q_0}. \tag{6}$$

- Under the CTL model, tidal evolution starting with identical orbital parameters (q_0, Q_0) forms a set of equivalent evolution tracks that follow the identical trajectory in a–e space and simultaneous in T_pt space, with T_p modulating the tidal evolution rate given by:

$$T_p = \frac{K_pM_*^2R_p^5}{M_p} \propto \frac{K_pM_*^2R_p^2}{\rho_p}. \tag{7}$$

- In comparison to the timescale of semi-major axis and eccentricity decay, the planetesimal reaches pseudo-synchronization

Equilibrium	
ω_{eq}	$\frac{2\cos\epsilon_p}{1+\cos^2\epsilon_p}\frac{f_2(e)}{(1-e^2)^{\frac{3}{2}}f_5(e)}n$ $\left[G(M_p+M_*)\right]^{\frac{1}{2}}\left(\frac{q_0+Q_0}{2q_0Q_0}\right)^{\frac{3}{2}}\frac{2\cos\epsilon_p}{1+\cos^2\epsilon_p}\frac{f_2(e)}{f_5(e)}$ $\mathrm{sgn}\left(\frac{\partial\omega_{eq}}{\partial e}\right)=\mathrm{sgn}(e)$
ϵ_{eq}	$\begin{cases}0 & 0\leq\epsilon_{p,0}<\frac{\pi}{2}\\ \pi & \frac{\pi}{2}<\epsilon_{p,0}\leq\pi\end{cases}$
Circularization	
e_{cir}	0
a_{cir}	$\frac{2q_0Q_0}{q_0+Q_0}$
ω_{cir}	n
ϵ_{cir}	ϵ_{eq}
Evolution trends	
a	$\mathrm{sgn}(\frac{da}{dt})=-\mathrm{sgn}(e)$ $\mathrm{sgn}(\frac{\partial\dot{a}}{\partial e})=-\mathrm{sgn}(e)$ $\frac{da}{dt}(e\rightarrow0)=0$
e	$\mathrm{sgn}(\frac{de}{dt})=-\mathrm{sgn}(e)$ $\mathrm{sgn}(\frac{\partial\dot{e}}{\partial e})=\mathrm{sgn}(e-0.658)$ $\frac{de}{dt}(e\rightarrow0)=\frac{de}{dt}(e\rightarrow1)=0$
ω_p	$\mathrm{sgn}(\frac{d\omega_p}{dt})=\mathrm{sgn}(\omega_{eq}-\omega_p)$
ϵ_p	$\mathrm{sgn}(\frac{d\epsilon_p}{dt})=\mathrm{sgn}(\epsilon_{eq}-\epsilon_p)$ $\mathrm{sgn}(\frac{\partial\dot{\epsilon}_p}{\partial\omega_p})=\mathrm{sgn}\left[\frac{2}{\eta_p}\omega_{eq}(\epsilon_p=0)-\omega_p\right]$
q	$\mathrm{sgn}(\frac{dq}{dt})=\mathrm{sgn}(e)$
Q	$\mathrm{sgn}(\frac{dQ}{dt})=-\mathrm{sgn}(e)$

Table 2. The equilibrium spin, obliquity, and the eccentricity, semi-major axis after tidal circularization under the CTL model, together with the general evolution trends (the signs of the differential equations) of the model. sgn(f) represents the sign of f, which is 1 if f is positive, 0 if f is 0 and -1 if f is negative. See appendices A and B for detailed analysis.

($\omega_p = \omega_{eq} \propto n$) and spin-orbit (mis)alignment ($\epsilon_p = \epsilon_{eq} = 0, \pi$) rapidly.

- The semi-major axis decay rate $|\frac{da}{dt}|$ and orbital period decay rate $|\frac{dT}{dt}|$ increase with eccentricity e, and hence declines during tidal evolution.
- The eccentricity decay rate $|\frac{de}{dt}|$ has its maximum at $e \approx 0.658$.
- A planetesimal evolves much faster under tide if it starts at a smaller pericentre distance (for an initially highly eccentric orbit, the analytical circularization timescale satisfies $\tau_{cir} \propto q_0^{7.5}$).
- The general trend of tidal evolution of a white dwarf-planetesimal system under the CTL model is the decay in eccentricity, semi-major axis and apocentre distance, the increase in the pericentre distance, accompanied with spin-orbit (mis)alignment and pseudo-synchronization.

2.2 The Roche limit

If the planetesimal is scattered too close to the white dwarf, the differential tidal force may lead to rapid disintegration of the body, in which case tidal evolution is irrelevant. The critical distance where the gravitational acceleration, the maximum acceleration provided by ultimate tensile strength, the centrifugal acceleration and the tidal acceleration add up to 0 is defined as the Roche limit (r_{Roche}). Within the Roche limit, the net acceleration leads to fracture of the body, referred to as tidal disruption. Tidal disruption ceases at the point the size of the constituent is reduced to the point where the ultimate tensile strength is sufficient to support the object. In this study, we only consider the planetesimals outside the Roche limit. We apply the model in Bear & Soker 2015; Brown et al. 2017; Brouwers et al. 2022, where the acceleration balance is investigated at the surface (an alternative model considering a fracture plane is discussed in Davidsson 1999), further incorporating the pseudo-synchronous spin of the planetesimal undergoing tidal evolution. The balance among the four accelerations for a spherical rigid planetesimal (we will extend our study to non-spherical bodies in Section 4.3) can be expressed as:

$$\frac{2GM_*R_p}{r_{Roche}^3} + \omega_p^2 R_p = \frac{GM_p}{R_p^2} + \frac{\sigma_s \pi R_p^2}{M_p}, \tag{8}$$

where σ_s is the ultimate tensile strength.

The Roche limit can be obtained by solving Eq.8:

$$r_{Roche} = \left[\frac{2GM_*}{\frac{4}{3}\pi G\rho_p + \frac{3\sigma_s}{4\rho_p R_p^2} - \omega_p^2}\right]^{\frac{1}{3}}. \tag{9}$$

Due to the fact that on the timescales of pseudo-synchronization ($\omega_p = \omega_{eq}$) and spin-orbit alignment ($\epsilon_p = 0, \pi$), a and e stays nearly constant, the necessary condition of avoiding tidal disruption after scattering of the planetesimal, $q_0 > r_{Roche,0}$ (with q_0 the initial pericentre distance and $r_{Roche,0}$ the initial Roche limit after scattering), can be obtained by substituting $\omega_p = \omega_{eq}(a_0, e_0, \epsilon_p = 0, \pi)$ (see Table 2 for the expression), and solve the following set of equations:

$$\begin{cases} |\omega_p| = \sqrt{\frac{4\pi G\rho_p}{3} + \frac{3\sigma_s}{4\rho_p R_p^2} - \frac{2GM_*}{r_{Roche,0}^3}} \\ |\omega_p| = \frac{f_2(e_0)}{(1-e_0^2)^{\frac{3}{2}} f_5(e_0)} n_0 \\ e_0 = \frac{Q_0 - r_{Roche,0}}{Q_0 + r_{Roche,0}} \end{cases}, \tag{10}$$

Eq.10 cannot be solved analytically. However, one can find an approximated solution using the fact that $r_{Roche,0} \ll Q_0$ ($e_0 \approx 1 - \frac{2r_{Roche,0}}{Q_0}$, $a_0 \approx \frac{Q_0}{2}$) usually applies:

$$|\omega_p| = |\omega_{eq,0}| \approx \frac{33}{40}\sqrt{2GM_*} r_{Roche,0}^{-\frac{3}{2}}, \tag{11}$$

and the Roche limit can be approximated as:

$$r_{Roche,0} \approx \left(\frac{3.36125 GM_*}{\frac{4}{3}\pi G\rho_p + \frac{3\sigma_s}{4\rho_p R_p^2}}\right)^{\frac{1}{3}}, \tag{12}$$

which has a maximum at $\rho_p = \frac{3}{4R_p}\sqrt{\frac{3\sigma_s}{\pi G}}$ and is independent of Q_0.

Due to the fact that the pericentre distance q increases while ω_{eq} decreases with tidal evolution (Section 2.1.2), the condition $q_0 \geq r_{Roche,0}$ is sufficient to avoid tidal disruption assuming that the properties of the object remain the same.

2.3 Summary

The physical processes considered in this study are summarized in Fig.1: planetesimals scattered to pericentre distances narrowly

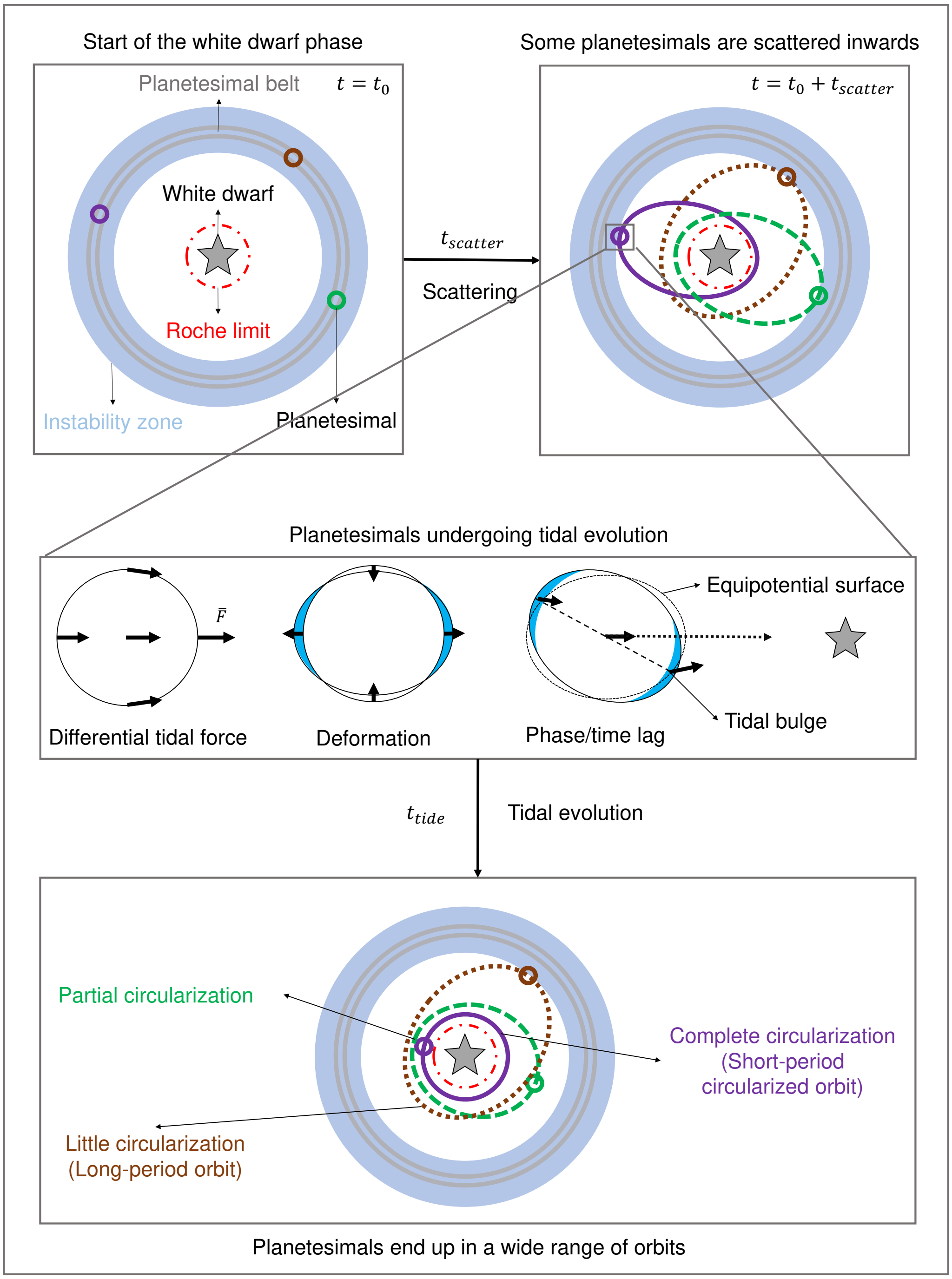

Figure 1. A schematic diagram of planetesimals scattered towards a white dwarf that evolve onto shorter-period orbits under tides (face-on view, not to scale). Three snapshots in time are presented: 1. at the start of the white dwarf phase (upper-left panel), 2. when the planetesimal is initially scattered (upper-right panel), and 3. after a given tidal evolution time (lower panel) where planetesimals evolve onto a wide range of orbits. The stages of tidal evolution can be categorized as: complete circularization (purple, small q_0, short-period circular orbit), partial circularization (green, moderate q_0) and little circularization (brown, large q_0, long-period highly eccentric orbit). The middle panel is a sketch of the tidal effect: 1. the white dwarf exerts a differential tidal force on the planetesimal (left), 2. the planetesimal is deformed, leading to the formation of tidal bulges (middle) and 3. the lag of tidal bulges relative to the equipotential surface (right) leads to dissipation of orbital energy.

avoiding tidal disruption experience strong tidal force, inducing tidal bulges that lag behind the equipotential surface, damping orbital energy, bringing these planetesimals to a wide range of orbits: 1. short-period circularized orbits (purple), 2. partially circularized orbits (green), 3. long-period orbits nearly unaffected by tidal effect (brown).

For identical two-body system properties, tidal evolution rate increases rapidly with the decreasing initial pericentre distance (Section 2.1.2). The initial pericentre distance q_0 and initial apocentre

Planetesimal	ρ_p (kg/m^3)	3000
	R_p (km)	100
	K_p (s)	1000
	C_p	$\frac{2}{5}$
	σ_s (Pa)	10^5
White dwarf	M_* ($M_\odot$)	0.6
Orbit	Q_0 (AU)	3
	$\omega_{p,0}$ ($\omega_{eq,0}(\epsilon_p = 0)$)	1
	$\epsilon_{p,0}$	0
	$P(q_0)$	$P(q_0) \propto q_0^{\frac{1}{2}}$

Table 3. The fiducial set of parameters used in this work to describe a planetesimal-white dwarf system undergoing tidal evolution. The choice of K_p is motivated by the tidal dissipation of typical rocky bodies (Lambeck 1977; Neron de Surgy & Laskar 1997; Bolmont et al. 2011; Clausen & Tilgner 2015; Barnes 2017; Rufu & Canup 2020; Sánchez et al. 2020; Bagheri et al. 2022). The choices of ρ_p and σ_s are motivated by the physical properties of chondrites (Ostrowski & Bryson 2019; Pohl & Britt 2020). The choice of white dwarf mass roughly corresponds to the peak of the observed white dwarf mass distribution (Kepler et al. 2007; Tremblay et al. 2016; Kepler et al. 2017).The initial apocentre of the planetesimals, Q_0, is set such their orbits did not enter the stellar envelope during the giant branches, i.e. slightly above the maximum size of the stellar envelopes of 1–3 $M_\odot$ stars with solar metallicity based on MESA isochrones and stellar tracks (MIST, Dotter 2016; Choi et al. 2016). The initial spin and obliquity are arbitrarily chosen to be their equilibrium values as they have little effect on the semi-major axis and eccentricity evolution (see Section 3.1.1).

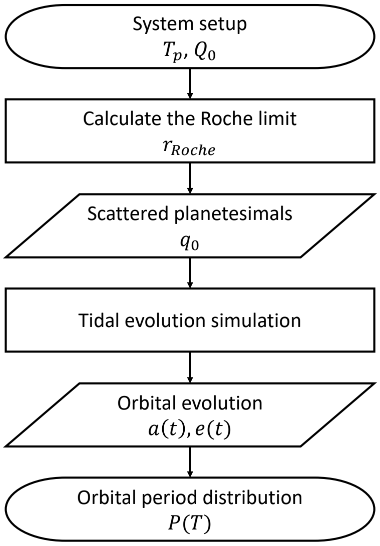

Figure 2. A flow chart presenting the method described in Section 2: 1. initial setup of a white dwarf-planetesimal system (two-body system properties T_p and initial apocentre distance Q_0), 2. compute the Roche limit (r_{Roche}), 3. imitate the scattering process via an initial pericentre (q_0) distribution whose lower limit is set by the Roche limit, 4. simulate the tidal evolution, 5. obtain the time evolution of orbital parameters ($a(t)$, $e(t)$), and 6. compute the resultant orbital period distribution.

distance Q_0 of the planetesimal after leaving the instability zone are shaped by the white dwarf planetary system, which comes with a wide range of architectures. Instead of simulating the dynamical processes delivering planetesimals close to the white dwarf, we introduce a power law probability density function (PDF) of q_0 of the planetesimal to imitate the effect of scattering: $P(q_0 \geq r_{Roche,0}) \propto q_0^\alpha$. We obtain a population of q_0 that the planetesimal is scattered to according to the PDF using the Metropolis algorithm with a sample size of 10^5. With the lower limit of q_0 set by the Roche limit, we set the upper limit to 0.012 AU, above which the planetesimal's orbital period can hardly decay below 1 yr within 1 Gyr, adding difficulties to observations. The default value of α chosen for this study is $\alpha = \frac{1}{2}$. We will discuss the choice of this PDF and the effect of different α in Section 4.2, and show that the resultant orbital period distribution is qualitatively insensitive to the assumed initial pericentre distribution. Q_0 physically represents the inner edge of the scattering zone, which may vary a lot among different systems. For planets as perturbers, Q_0 depends on planet-planet interactions (e.g., scattering, resonances) and planet-star interactions (e.g., tidal interaction, common-envelope evolution), and is not necessarily equivalent to the semi-major axis of a planet would have at the end of the asymptotic giant branch assuming adiabatic orbital expansion under stellar mass loss. We will discuss the effect of Q_0 on the circularization timescale and the orbital period distribution in Section 3.1.2 and Section 4.2.

The default setup of the white dwarf-planetesimal system is listed in Table 3, unless otherwise stated (see the caption for the motivation of choices). The properties of exoplanetary bodies, especially the tidal dissipation efficiency quantified by $K_p = 3k_2\Delta t$, are poorly constrained, and may be altered during tidal evolution. Knowing the tidal evolution time and the tidal evolution stage relative to the initial condition ($a(t)$, $e(t)$, q_0, Q_0) is insufficient to disentangle the parameters within T_p (Eq.7). Furthermore, the constituents of T_p are not necessarily independent variables. Hence, it is more appropriate to consider T_p as a whole. However, we will still investigate the effect of varying the individual constituents of T_p independently (e.g., density, radius) for illustrative purpose. On the other hand, as is mentioned in Section 2.1.2, planetesimals starting with same q_0 and Q_0 would have identical orbital parameters at identical $T_p t$. Therefore, for a realistic T_p that is k times the assumed value in this study, one can obtain the realistic counterparts of our simulation results by substituting $\frac{t}{k}$ to t.

With the initial orbital parameters and the properties of the planetesimal-white dwarf system, one can simulate the orbital evolution of a planetesimal.

The method is summarized in Fig.2:

(i) We setup the properties of the two-body system.

(ii) We compute the Roche limit as the lower limit of initial pericentre distance of planetesimals.

(iii) We use the Metropolis algorithm to generate a sample of initial pericentre distance outside the Roche limit according to the power law probability density function, $P(q_0 \geq r_{Roche,0}) \propto q_0^\alpha$.

(iv) We simulate the tidal evolution of sample planetesimal-white dwarf systems by linearly interpolating within a pre-simulated grid of tidal evolution tracks for a range of initial pericentre distances.

(v) We obtain the orbital evolution of planetesimals around white dwarfs, from which we deduce the orbital period distribution.

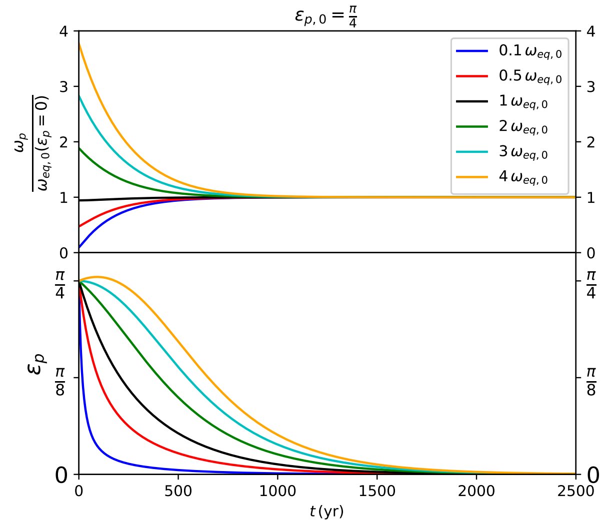

Figure 3. The tidal evolution of the spin (ω_p, upper panel) and obliquity (ϵ_p, lower panel) of the planetesimal under the CTL model for an initial obliquity of $\frac{\pi}{4}$. We choose $q_0 = 0.01$ AU. Each colour corresponds to a different initial spin expressed as a multiple of the initial equilibrium spin with 0 obliquity $\omega_{eq,0}(\epsilon_p = 0)$. a and e remain identical on the timescale of this plot. Other choice of free parameters are listed in Table 3.

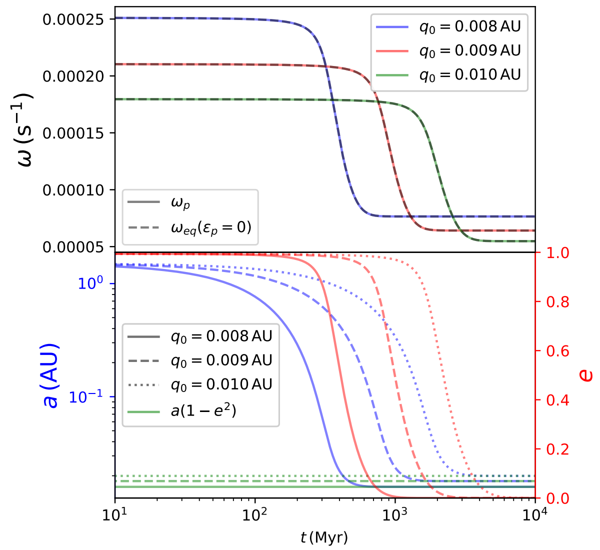

Figure 4. The tidal evolution of ω_p (solid lines), ω_{eq} (black dashed lines) in the upper panel, which perfectly overlap with each other, and the evolution of a (blue lines, left axis), and e (red lines, right axis) in the lower panel, for $q_0 = 0.008, 0.009, 0.010$ AU. The green lines are $a(1-e^2)$ (left axis) for the corresponding q_0. Other free parameters are listed in Table 3.

3 RESULTS

3.1 Tidal evolution under the CTL model

To obtain the orbital period of a planetesimal at a given snapshot in time, we need to model its orbital evolution. In this section we model the tidal evolution tracks of sample systems, comparing them to the analytical analysis in 2.1.2 (3.1.1), and investigate the parameter-dependence of tidal circularization timescale (3.1.2).

3.1.1 Tidal evolution tracks

In Fig.3, we plot the evolution of spin, ω_p (upper panel) and obliquity, ϵ_p (lower panel) at $q_0 = 0.01$ AU for different initial spins (expressed as the multiple of $\omega_{eq,0}(\epsilon_p = 0)$) over 2500 yr. The key features are summarized below:

- Spin and obliquity converge to their equilibrium values on similar timescales (~ 1000 yr), within which semi-major axis and eccentricity, which decay on much longer timescales (~ 1 Gyr, see Fig.4, lower panel) remain unchanged.
- Spin and obliquity converge to the common equilibrium values, $\omega_{eq,0}(\epsilon_p = 0)$ and 0, respectively, insensitive to the initial spin and obliquity.
- A smaller initial spin rate corresponds to a faster obliquity decay (lower panel, from the blue line to the orange line).
- For large initial spin, there exists temporary increasing obliquity opposite to the general declining trend (lower panel, orange line).

These features are consistent with the deduced properties of the CTL model. The key deduction from spin and obliquity evolution is that the choice of initial spin and obliquity has little effect on the tidal evolution in a–e space.

In Fig.4, we plot the evolution of ω_p (solid lines) and ω_{eq} (black dashed lines) for 3 different q_0: 0.008 AU (blue), 0.009 AU (red) and 0.010 AU (green) for 10 Gyr in the upper panel, together with the corresponding evolution of a and e in the lower panel. In the upper panel, the persistent overlap of the solid lines (ω_p) and the dashed lines ($\omega_{eq}(\epsilon_p = 0)$) indicates that a planetesimal effectively remains in the pseudo-synchronization and spin-orbit alignment state when considering the evolution in a and e.

The green lines in the lower panel representing $a(1-e^2)$ (left axis) are horizontal, and perfectly overlap with the value that the blue lines (a) converge to, indicating conservation of orbital angular momentum throughout tidal evolution, consistent with Section 2.1.2. In other words, the initial orbital parameters, q_0 and Q_0, determine the a–e relation during tidal circularization and the semi-major axis after circularization.

On the other hand, as is shown in the lower panel of Fig.4, the convergence of eccentricity always lags behind that of the semi-major axis, which is consistent with conservation of orbital angular momentum (Eq.6): $\frac{da}{a} = \frac{2e^2}{1-e^2}\frac{de}{e}$, such that $\frac{da}{a} \gg \frac{de}{e}$ at large e and that $\frac{da}{a} \ll \frac{de}{e}$ at small e (or, note that $|\frac{da}{dt}|$ decays monotonically towards $e \longrightarrow 0$ to 0, while $|\frac{de}{dt}|$ decays from its maximum, at $e \approx 0.658$, towards both $e \longrightarrow 0$ and $e \longrightarrow 1$, to 0, Section 2.1.2). Consequently, an orbit is effectively circularized in terms of its orbital period when the eccentricity is small ($e \lesssim 0.01$ in Fig.4), and it takes much longer to reach the true circularization point $e = 0$.

With the increase in q_0 from 0.008 AU to 0.010 AU, the time required for the semi-major axis (blue lines) to converge increases rapidly from $\sim$ 700 Myr to $\sim$ 4000 Myr, roughly consistent with $\tau_{cir} \sim \left|\frac{a}{\dot{a}}\right|_0 \propto q_0^{7.5}$ (Appendix B). Furthermore, at same t, the orbital period difference of two planetesimals starting at different q_0 initially increases and then decays during tidal evolution, reaching a constant after both planetesimals are circularized.

3.1.2 Tidal cirularization timescale

If planetesimals are to evolve onto (nearly) circular orbits around white dwarfs due to tides, this evolution must occur well within the white dwarf cooling age. In this section we simulate the variation in circularization timescale (τ_{cir}) in response to the physical properties

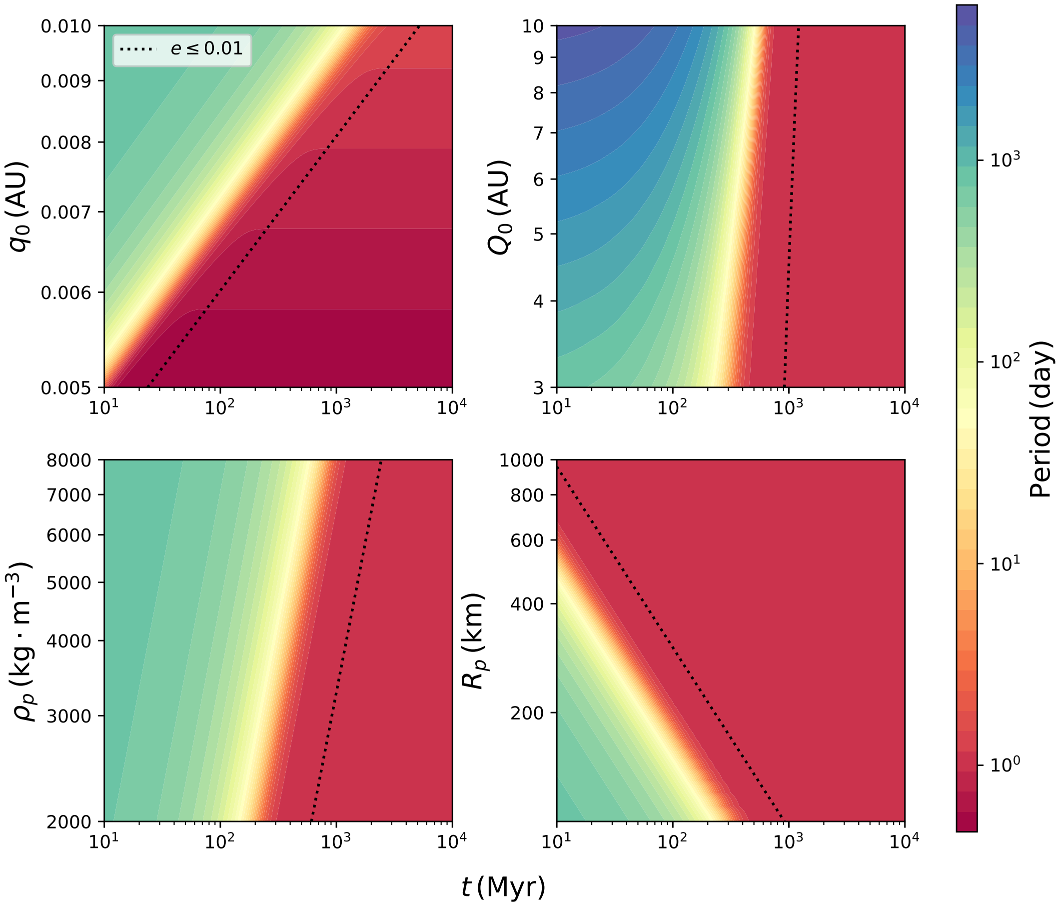

Figure 5. The contour plots of the orbital period of the planetesimal in t–q_0 space (upper-left panel), as well as its counterparts in t–Q_0 space (upper-right panel), t–ρ_p space (lower-left panel) and t–R_p space (lower-right panel) at a fixed $q_0 = 0.008$ AU. The axes are all on the logarithmic scale. Other free parameters are identical to those in Table 3. The dotted lines are the circularization lines, at the right of which $e \leq 0.01$ is satisfied.

$\frac{\partial \log \tau_{cir}}{\partial \log q_0}$	$\frac{\partial \log \tau_{cir}}{\partial \log Q_0}$	$\frac{\partial \log \tau_{cir}}{\partial \log \rho_p}$	$\frac{\partial \log \tau_{cir}}{\partial \log R_p}$
7.8	0.2	1.0	-2.0

Table 4. The gradient of circularization lines on the logarithmic scale in Fig.5.

of the planetesimal and the initial orbital parameters. We consider planetesimal size and density as independent variables for demonstration only, which is not necessarily realistic.

In Fig.5, we plot the orbital period evolution of the planetesimal in t–q_0 (upper-left panel), t–Q_0 (upper-right panel), t–ρ_p (lower-left panel) and t–R_p (lower-right panel) space. The dotted lines are the circularization lines under the condition $e \leq 0.01$, at the right of which the planetesimal's orbit is considered to be effectively circularized. We do not use $e = 0$ as the condition of circularization because a nearly circularized orbit is non-distinguishable from, but is reached much earlier than its circularized counterpart, as mentioned in Section 3.1.1. The gradients of circularization lines on the logarithmic scale are summarized in Table 4. We find out that these gradients are not sensitive to the numerical condition of circularization (for instance, the computed gradients are almost identical when setting the threshold to be $e \leq 10^{-4}$ instead) and other free parameters (for instance, Q_0 in the upper-left panel, q_0 in upper-right and lower panels).

Clearly, the gradient of the circularization line in the upper-right panel, corresponding to $\frac{\partial \log \tau_{cir}}{\partial \log q_0} \approx 7.8$, far exceeding the magnitude of others, indicating that the initial pericentre distance q_0 dominates the circularization timescale over other free parameters. The empirical relation $\tau_{cir} \propto q_0^{7.8}$ (with the scaling insensitive to a wide range of Q_0 and T_p) is roughly consistent with the analytically computed circularization timescale $\left|\frac{a}{\dot{a}}\right|_0 \propto q_0^{7.5}$ (the difference originates from the fact that the analytical expression is obtained by expanding $\frac{a}{\dot{a}}$ at $t = 0$, which becomes less accurate as the orbital parameters deviate from their initial values under tidal evolution). At any snapshot in time, the orbital period of the planetesimal decreases monotonically with q_0. If a planetesimal starts at a smaller pericentre distance, it would circularize much more rapidly and to a shorter orbital period.

The Roche limit of the planetesimal with the default properties (Table 3) is 0.00456 AU, corresponding to a minimum circularization timescale of $\sim$ 10 Myr. Therefore, for a white dwarf with a cooling age of 1 Gyr, there may exist tidally circularized planetesimals unless the tidal dissipation of exoplanetary bodies quantified by T_p (Eq.7) is $\gtrsim$ 100 times smaller than our fiducial value (Table 3). In a regime where ρ_p can be considered as an independent variable, and when the self-gravity far exceeds the material strength, Eq.12 is reduced to $r_{Roche} \propto \rho_p^{-\frac{1}{3}}$. Therefore, the minimum circularization timescale

($\tau_{cir} \propto r_{Roche}^{7.8}\rho_p$) is roughly proportional to $\rho_p^{-1.6}$, such that increasing planetesimal density from 3000 kg/m^3 to 4000 kg/m^3 reduce the minimum circularization timescale to $\sim$ 6 Myr.

Among the free parameters investigated in this section, the dependence of τ_{cir} on Q_0 is the weakest, as is shown in the nearly vertical circularization lines in the upper-right panel of Fig.5 corresponding to $\tau_{cir} \propto Q_0^{0.2}$. However, the orbital period of partially circularized planetesimals (at the left of the circularization lines) are increasingly affected by Q_0 at an earlier tidal evolution stage, where a larger Q_0 corresponds to a a and hence larger $T(t)$.

The delayed circularization with the increase in ρ_p in the lower-left panel, with $\tau_{cir} \propto \rho_p$, and the accelerated tidal circularization with increasing planetesimal size in the lower-right panel, with $\tau_{cir} \propto R_p^{-2}$, are consistent with the fact that $\dot{a}$ and $\dot{e}$ are proportional to $T_p \propto R_p^2\rho_p^{-1}$.

Combining the scaling relations above, we obtain an empirical scaling relation for the circularization timescale of planetesimals around white dwarfs under the CTL model:

$$\begin{aligned}\tau_{cir} \approx 5000\frac{1000\,\mathrm{s}}{K_p}\left(\frac{0.6\,M_\odot}{M_*}\frac{100\,\mathrm{km}}{R_p}\right)^2\frac{\rho_p}{3000\,\mathrm{kg/m^3}} \\ \times\left(\frac{q_0}{0.01\,\mathrm{AU}}\right)^{7.8}\left(\frac{Q_0}{3\,\mathrm{AU}}\right)^{0.2}\,\mathrm{Myr}.\end{aligned} \tag{13}$$

3.2 Probability distribution of orbital period

This section predicts the probability distribution of the orbital period for a planetesimal evolving under tidal interactions (which can be equivalently interpreted as the orbital period distribution of a population of planetesimals with identical properties and tidal evolution times). The orbital (transiting) period is the key observable to compare with. We note here that the probability distribution of a given planetesimal (given planetesimal population) is different if plotted in terms of the planetesimal's orbital period rather than semi-major axis, on linear rather than logarithmic scale (see Appendix C).

We investigate the probability distribution in the period space and on the logarithmic scale for orbital periods $\leq$ 1 year, since it is more natural to compare between $P(0.9\,\mathrm{day} \leq \mathrm{T} \leq 1.1\,\mathrm{day})$ to $P(90\,\mathrm{day} \leq \mathrm{T} \leq 110\,\mathrm{day})$, instead of comparing between $P(0.9\,\mathrm{day} \leq \mathrm{T} \leq 1.1\,\mathrm{day})$ to $P(99.9\,\mathrm{day} \leq \mathrm{T} \leq 100.1\,\mathrm{day})$.

In Fig.6, we show 2 snapshots in tidal evolution time: 100 Myr and 500 Myr of the probability distribution of planetesimal's orbital period limited to $T \leq 1$ yr (histogram, left axis) on the logarithmic scale, with the zoom-in plot for the short period orbits ($T \leq 1$ day) in the linear space. Note that T_p and t are entangled such that the distribution at a tidal evolution time of 100 Myr can be equivalently understood as a distribution at $t = 500$ Myr but for a planetesimal with T_p that is 5 times weaker (tidal evolution is simultaneous in $T_p t$ space, 2.1.2). The probability distribution is normalised such that at $t = 100$ Myr, the probability within the cut-off period, 1 yr, adds up to 1. The dashed line is the minimum circularization period ($P_{cir}(r_{Roche})$) computed from Eq.6 and Eq.10. The solid and dotted lines are the orbital eccentricity a planetesimal would have at current orbital period, at a tidal evolution time of 100 Myr and 500 Myr, respectively.

The key features of Fig.6 are summarized below:

(i) A peak of the probability distribution presents near the transition between (nearly) circularized and partially circularized orbits ($\sim$ 10 hr–1 day): an enhanced probability for the planetesimal to reside on a (nearly) circularized orbit.

(ii) There is a probability valley after the peak: low probability for the planetesimal to reside in a partially circularized orbit with an orbital period between $\sim$ 1 day and $\sim$ 100 day.

(iii) There is an increasing tail towards longer-period highly eccentric orbits ($\gtrsim$ 100 day).

(iv) As the time of tidal evolution increases (the hatched histogram versus the blue histogram), the peak of the probability distribution shifts towards longer period and the contributions from the (nearly) circularized orbits to the probability distribution increases.

(v) The probability distribution of the (nearly) circularized orbits is uniform in the linear space (zoom-in plot) and hence linear in the logarithmic space.

Notably, the pile-up at short-period nearly circularized orbits and long-period highly eccentric orbits ((i), (ii) and (iii)) is a natural consequence of the tidal model and the utilization of logarithmic scale, rather than the initial pericentre distribution. This is shown in Fig.7, which illustrates that a given bin-width in logarithmic period space (fixed $\frac{\Delta T}{T}$) covers a wider range of q_0 towards short-period nearly circularized orbits and long-period highly eccentric orbits under tidal evolution. Fig.7 is equivalent to a cumulative distribution for a uniform distribution in q_0 and the orbital period distributions of tidally evolved planetesimals are strongly shaped by the pile-up illustrated in Fig.7. The physical origin of this pile-up is briefly explained in Appendix C, from which we can deduce that, as long as the realistic tidal evolution remains qualitatively similar to the predictions of the CTL model in terms of:

- semi-major axis decay generally decelerates along the tidal evolution track, converging to 0 at $e = 0$,
- a planetesimal closer to the white dwarf at its pericentre undergoes more rapid tidal evolution,

the qualitative features (i) (ii) and (iii) of the orbital period distribution should persist, regardless of the assumptions regarding the initial pericentres (see Section 4.2).

On the other hand, the tidal model and the planetesimal population (e.g., initial pericentre distribution, physical properties) can affect the orbital period distribution quantitatively. The inner edge of the orbital period distribution is an indication of the Roche limit, constraining the physical properties such as density and tensile strength of the planetesimal. The position of the peak at short-period, indicating the transition from near-circular to eccentric orbits not only indicates the tidal evolution stage of the system but also illustrates the maximum pericentre distance where a planetesimal scattered to can be tidally circularized within a given timescale. The peak for nearly circularized planetesimals, if presenting at a larger orbital period, indicating a later tidal evolution stage under the CTL model, i.e., longer tidal evolution time/stronger tidal interactions ((iv)), because CTL model predicts that a planetesimal starting with a larger q_0 circularizes slower to a longer orbital period. The time evolution of the orbital period distribution is affected by the dependence of tidal model on the initial pericentre distance. The orbital period distribution of nearly circularized orbit, as well as the fraction of nearly circularized to partially circularized orbits, is related to the initial pericentre distribution. For instance, our choice of PDF $P(q_0) \propto q_0^{\frac{1}{2}}$ corresponds to an uniform orbital period distribution in the linear space (linear in logarithmic period space) for nearly circularized planetesimals ((v), Appendix C). To summarize, the qualitative features of the orbital period distribution: peak at short-period nearly circularized orbit and an increasing tail towards long-period highly eccentric orbits persist for any tidal evolution that is qualitatively similar to the CTL model, while the quantitative details of the distribution probes the

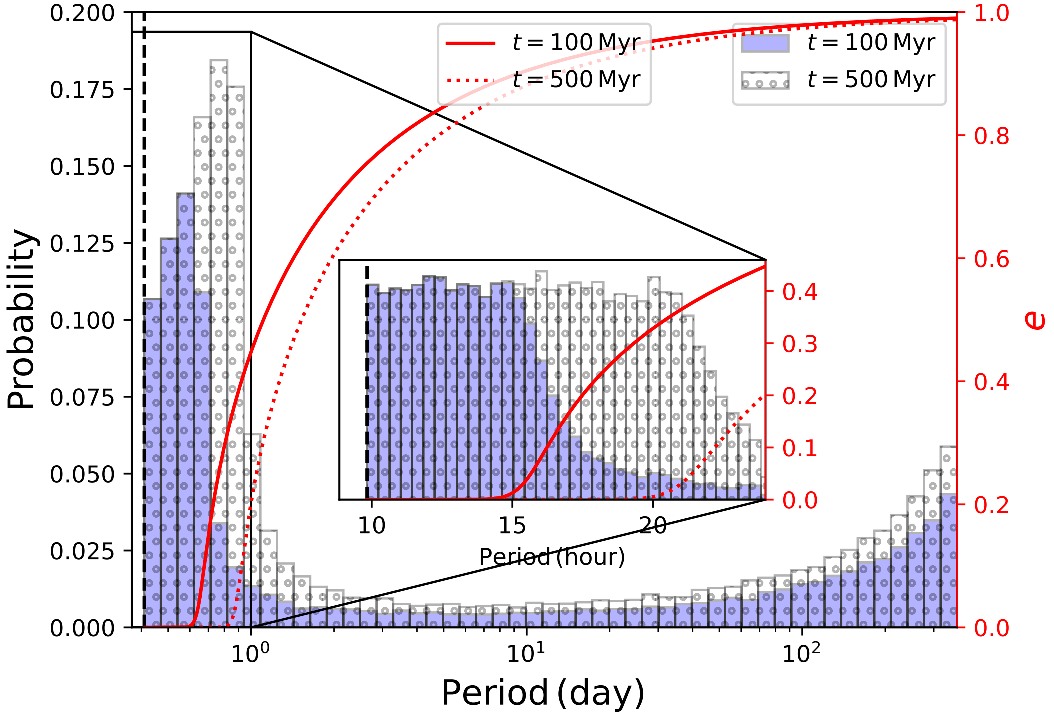

Figure 6. The simulated normalised probability distribution of the planetesimal's orbital period (left axes, histogram) and eccentricity (right axes, lines) within 1 yr on the logarithmic scale, at a tidal evolution time of 100 Myr (blue histogram, solid line) and 500 Myr (hatched histogram, dotted line), together with the zoom-in plot for orbital period less than 1 day on the linear scale. The free parameters are listed in Table 3.

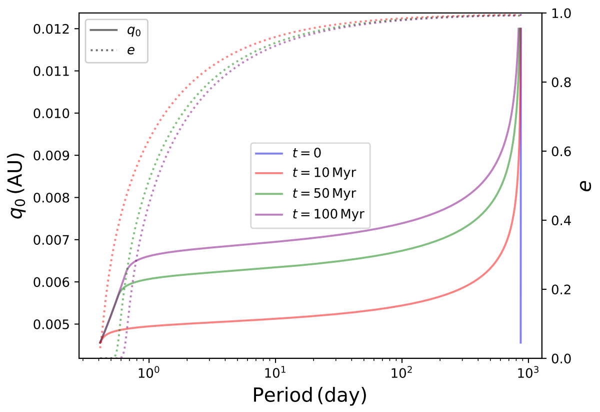

Figure 7. The orbital period and orbital eccentricity a planetesimal scattered to q_0 would have at 4 snapshots in time for a range of q_0. The free parameters are identical to those in Table 3.

tidal model, as well as the population of planetesimals undergoing tidal evolution.

4 DISCUSSION

This paper studies an alternate pathway for planetesimals scattered close to the white dwarf. While planetesimals scattered interior to the Roche limit are tidally disrupted and accreted by the white dwarf, planetesimals scattered just outside the Roche limit may undergo tidal circularization. These tidally evolved planetesimals potentially span a wide range of orbital periods at a given snapshot in time (Fig.8). These planetesimals may be responsible for transits observed around white dwarfs.

The observed light curves for the white dwarfs with photometric variability are not consistent with the transit of an intact body, but do contain periodic signatures that could be explained by active dust production associated with planetary bodies (Vanderburg et al. 2015; Veras et al. 2017; Duvvuri et al. 2020). If the observed periods correspond to the orbits of planetesimals, this work presents a mechanism for planetesimals to arrive on short period orbits. Mechanisms that allow planetesimals on short period orbits to produce photometrical variability in white dwarfs will be the subject of Paper II in this series (see Vanderburg et al. 2015; Veras et al. 2017; Duvvuri et al. 2020 for existing models).

Planetesimals that are tidally evolved outside the Roche limit and their counterparts tidally disrupted inside the Roche limit may coexist, with the ratio between them potentially varying in different systems and different evolutionary stages. The key test of this model is the distribution of orbital periods in the population of white dwarfs with observed transits. In this section, we firstly discuss the limitations of the model that affect the predictions made regarding the orbital period distributions of planetesimals shaped by tidal evolution, starting with the tidal model (Section 4.1) and the choice of the initial conditions, which dominate the subsequent tidal evolution (Section 4.2). Our model predictions are then compared to the current observations (Section 4.4 and 4.3), before the implications of an alternative pathway for planetesimals to evolve in white dwarf planetary systems are discussed (Section 4.5).

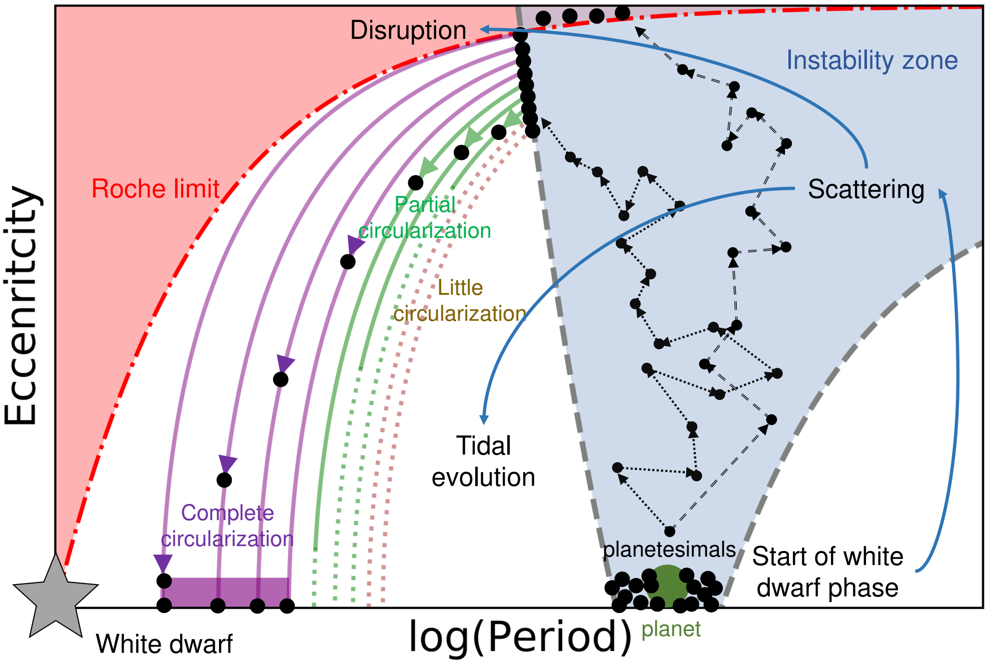

Figure 8. A schematic illustrating two potential pathways to white dwarf pollution from planetesimals scattered inwards by planets. Planetesimals that are scattered interior to the Roche limit are tidally disrupted and accreted. Planetesimals scattered outside the Roche limit evolve under tides, potentially leading to a wide range of orbits around the white dwarf.

4.1 Tidal model

Although the details of the prediction for the distribution of orbital periods of planetesimals orbiting white dwarfs depends on how white dwarf-planetesimal systems evolve under tide, the general properties of the distribution, most notably the pile-up of planetesimals on short-period (nearly) circularized orbits (which originates from the decelerating decay rate of orbital period during tidal circularization) is robust. Here we discuss the limitations in our understanding of how tides act on planetesimals and how these influence the results presented in this work.

In this study, we utilize the CTL model, which assumes an equilibrium tidal bulge lags behind the equipotential surface for a constant time. The CTL model is a simplified tidal model equivalent to a rheology where the induced tidal response is proportional to the corresponding tidal forcing frequency, such that the summed tidal dissipation efficiency of all forcing frequencies can be characterized by a single proportionality constant (e.g., K_p in this study). On one hand, high-eccentricity tidal evolution may be fundamentally different from its low-eccentricity counterparts because high-eccentricity tidal interactions mainly occur near the pericentre where an orbital averaged description as is the case for the CTL model may become inaccurate, and tidal dissipation may originate from different physics as is described by the CTL model (for instance, excitation and dissipation of oscillation modes for gas giants and stars) (Press & Teukolsky 1977; Moe & Kratter 2018; Vick et al. 2019; Glanz et al. 2022; Rozner et al. 2022; Vick et al. 2019; Veras & Fuller 2020).

On the other hand, for realistic rheologies, the dependence of tidal response on the forcing frequency may no longer lie in the linear regime as is the case for the CTL model (Makarov & Efroimsky 2013; Noyelles et al. 2014; Storch & Lai 2014; Boué & Efroimsky 2019; Veras et al. 2019; Vick et al. 2023). Furthermore, a stable pseudo-synchronization state may not present at all orbital parameters (Makarov & Efroimsky 2013; Storch & Lai 2014; O'Connor & Lai 2020; Vick & Lai 2020), making the Roche limit more uncertain and tidally-induced rotational fission possible. Furthermore, thermal evolution of the planetesimal under tidal heating may alter its rheology, and hence the distribution of tidal energy inside the body, tidal response, as well as the Roche limit (Tobie et al. 2005; Beuthe 2013; Zahnle et al. 2015; Seligman et al. 2024), adding complexities to the physical picture, for instance, runaway melting (tidal response increases with the degree of melting Seligman et al. 2024), thermal regulation (tidal response decreases with the degree of melting Zahnle et al. 2015), re-triggered tidal disruption (weakening ultimate tensile strength, increasing degree of deformation, see 4.3) and thermal destruction (Veras & Fuller 2020). Notably, although tidal response (for instance, T_p in the CTL model) and tidal evolution time are degenerate in terms of the orbital parameters (for instance, orbital period), the thermal history is potentially non-degenerate (rapid heating versus slow heating). A coupled thermal-tidal evolution model is required to properly model the tidal circularization of planetesimals around white dwarfs properly, which is beyond the scope of this study.

The most profound effect of the uncertainties in the tidal model is whether the tidal circularization timescale for planetesimals are so long that planetesimals can hardly circularize under tides within the cooling age of the white dwarfs. If tidal circularization is impossible throughout the allowed parameter space, the orbital period distribution in Fig.6 is truncated before the orbital eccentricity approaches 0, such that the probability distribution may increase monotonically towards longer orbital period and the peak towards the short period (nearly) circularized orbits does not present (Appendix D). Conversely, at a given tidal evolution time, as long as there exists a parameter space where a planetesimal can become nearly tidally circularized, we do not expect a qualitative difference in the observed orbital period distribution from Fig.6, whose general features are shaped by the qualitative behaviours of the tidal model (see Section 3.2), although the strength of the features, for instance, the height and position of the peak at nearly circularized orbits, can vary.

4.2 Population of scattered planetesimals

Given the large potential range in the ways that planetesimals can be perturbed inwards from an outer planetary system, it is impossible to constrain the exact population of scattered planetesimals. The population of scattered planetesimal is an important input for the model here, but we will show that the resultant orbital period distribution is qualitatively insensitive to the relevant free parameters.

The assumed free parameters associated with the scattered planetesimal population around the white dwarf are:

- initial pericentre distance distribution (the likelihood and time taken of being scattered to a pericentre distance),
- initial apocentre distance (inner edge of the instability zone),
- property of white dwarf-planetesimal systems (T_p and r_{Roche}),
- tidal evolution time (the difference between cooling timescale of the white dwarf and scattering timescale, degenerate with T_p).

In this work we arbitrarily choose a power law PDF to describe the initial pericentre distribution, motivated by numerical simulations of scattering (Rodet & Lai 2024). We also note that a realistic initial pericentre distribution can be approximated as a power series via Taylor expansion at small q_0. By investigating the resultant orbital period distributions corresponding to single power law PDFs of q_0, we can recover the commonalities of a realistic orbital period distribution (with the latter a linear combination of the former). The power series should not be dominated by terms with large positive exponents as white dwarf pollutants, which potentially correspond to scattering into the Roche limit ($q_0 < r_{Roche}$), is not rare (Zuckerman et al. 2003, 2010; Koester et al. 2014; Wilson et al. 2019; O'Brien et al. 2023, 2024; Manser et al. 2024). The exponents are not necessarily integers as the realistic PDF may already contain a power law(s).

The tidal evolution stage of the planetesimal is quantified by $T_p t$, such that we cannot distinguish a planetesimal with strong tidal response but evolves for a short time from its counterpart with weak tidal response but evolves for a long time. When we vary the tidal evolution time as a free parameter, one can equivalently consider that we vary T_p (or both T_p and t provided that $T_p t$ stays the same).

The effect of each parameter on the probability distribution is plotted in Fig.9 and summarized below:

- Most importantly, varying the free parameters listed above do not affect the qualitative behaviours of the resultant orbital period distribution: the presence of a peak at the short-period nearly circularized orbit (~ 10 hr–1 day) and the increasing tail towards long-period highly eccentric orbits (~ 100 day) on the logarithmic scale. Therefore, these features should persist after a linear combination of individual orbital period distributions corresponding to different power law q_0 distributions and different sets of free parameters.
- If the planetesimal is scattered earlier and experiences longer tidal evolution/evolves faster under tide, there is a higher probability for short-period (nearly) circularized orbits (upper-left panel).
- If the planetesimal leaves the scattering zone at a larger apocentre distance, the probability ratio of being on a (nearly) circularized orbit to its counterpart of being on a partially circularized orbit increases (upper-right panel).
- Increasing the density alone, which reduces the Roche limit, extends the allowed initial pericentre distance towards smaller values where tidal circularization is much faster, hence shifting the orbital period distribution towards shorter orbital period with larger contributions from the (nearly) circularized orbits (lower-left panel).
- Including a density/Roche limit distribution of the scattered planetesimal leads to a decaying tail towards the shortest orbital period that is only reachable by the planetesimals with large density/small Roche limit (lower-left panel, black solid line, also see Fig.11).
- The initial pericentre distance distribution has non-negligible impact on the orbital period distribution quantitatively: the contributions from the (nearly) circularized orbits to the probability distribution becoming smaller with a decreasing likelihood of being scattered to a smaller pericentre distance; but not qualitatively (lower-right panel, see Appendix E for other forms of distributions).

We acknowledge that when tidal circularization is too slow, the cumulative distributions do not necessarily start at the circularization period of a planetesimal scattered to the Roche limit as is the case in Fig.9. Instead, it may truncate (reach 0) at a longer orbital period and the peak at short-period (nearly) circularized orbits does not present (Appendix D).

4.3 Tidal disruption or tidal circularization?

Planetesimals scattered sufficiently close to the white dwarf are torn apart by the differential tidal forces. This work focuses on those planetesimals scattered insufficiently close to be torn apart, but sufficiently close for tidal forces to circularize them.

This work assumes that the Roche limit delineates the minimum pericentre of a planetesimal to escape tidal disruption. As planetesimals scattered to highly eccentric orbits tidally circularize to an semi-major axis around twice their initial pericentre distance ($2q_0$, Eq.6) and the circularization timescale of the planetesimal follows $\tau_{cir} \propto q_0^{7.8}$ (Section 3.1.2), the minimum orbital period a planetesimal can circularize to, and the minimum time required for tidal circularization, are closely related to the lower limit of q_0: the Roche limit (r_{Roche}). Here we discuss the validity of this assumption and its implications for the model predictions.

In the previous sections, we estimate the Roche limit assuming that the planetesimal possesses an ultimate tensile strength of 0.1 MPa (Table 3), roughly corresponding to the lower limit of the measured meteroites samples (Pohl & Britt 2020). We now discuss the effect of this parameter choice, together with the uncertainties in the ultimate tensile strength, and propose potential scenarios involving the variations of the r_{Roche} during tidal evolution.

In Fig.10, we plot the minimum orbital period a planetesimal with $R_p = 100\,\mathrm{km}$ can circularized to without undergoing tidal disruption (T_{min}), a representation of the Roche limit, as a function of planetesimal density (ρ_p) and ultimate tensile strength (σ_s). We stress that T_{min} is insensitive to Q_0 (Eq.12) and M_* ($T_{min} \propto M_*^{-\frac{1}{2}} r_{Roche}^{\frac{3}{2}}$ and $r_{Roche} \propto M_*^{\frac{1}{3}}$) since $r_{Roche} \ll Q_0$. At $\sigma_s \lesssim 0.1\,\mathrm{Mpa}$, the planetesimal is in the self-gravity dominant regime where T_{min} is nearly independent of σ_s, above which the increase in σ_s can significantly reduce T_{min}. Fig.10 shows that an orbital period below ~ 6 hr can hardly be explained by a tidally circularized planetesimal with high density alone: ultimate tensile strength is always required to avoid tidal disruption.

The hatched rectangular regions in Fig.10 corresponds to the measured values of Solar System ordinary chondrites (Pohl & Britt 2020),

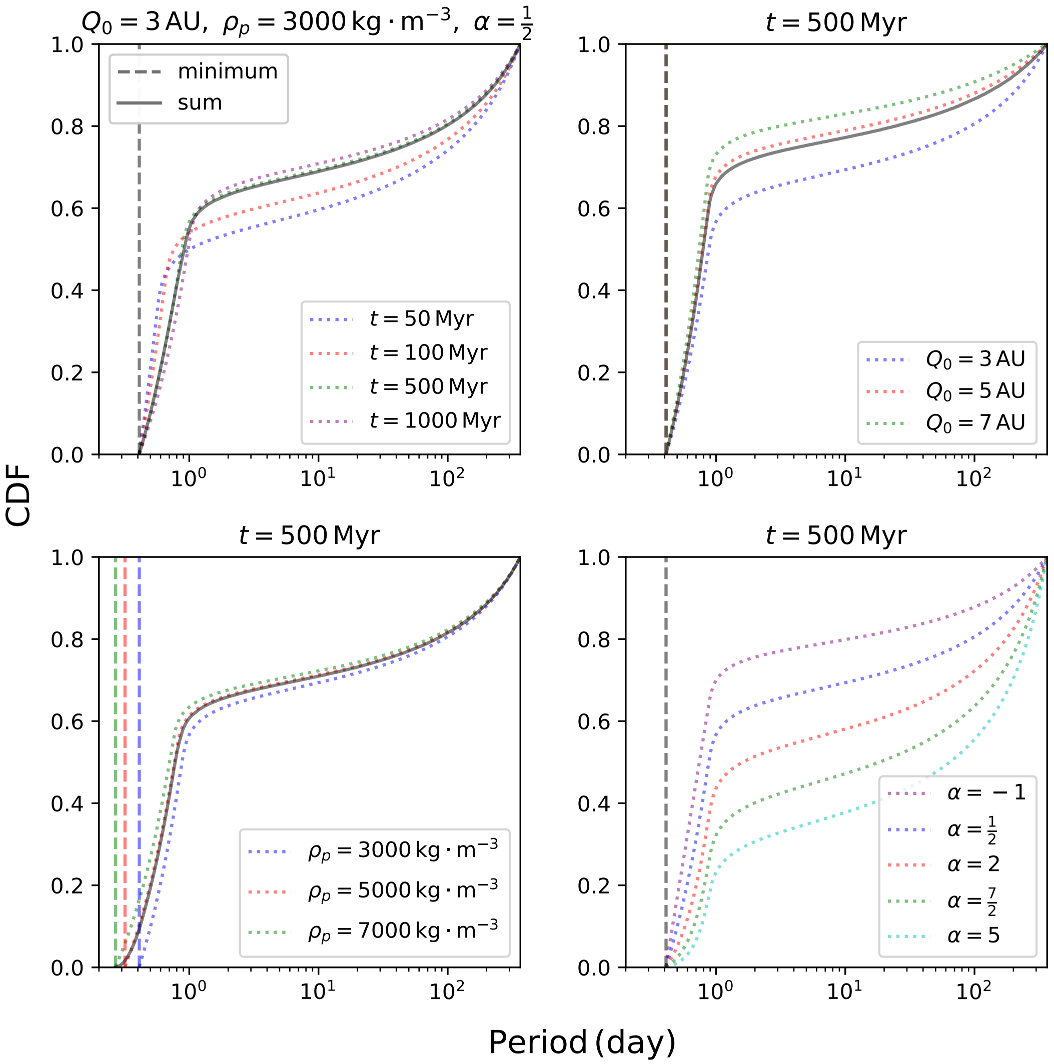

Figure 9. The cumulative distribution of planetesimal's period within 1 year for different evolution time (upper-left panel), initial apocentre distance (upper-right panel), density (lower-left panel) and initial pericentre distace distribution (lower-right panel). The default free parameters are identical to those in Table 3 unless otherwise stated. The dashed lines are the minimum circularization period obtained from Eq.6. The black solid lines are the CDFs obtained by summing the distribution for different tidal evolution time, initial apocentre distance and density uniformly within the range of the legend of each subplot.

which are the most abundant meteorites and may originate from main belt asteroids (Nesvorný et al. 2009; Nedelcu et al. 2014). A transiting period around/above the predicted T_{min} of ordinary chondrites, $T \gtrsim 6\,\mathrm{hr}$, can be explained by a tidally circularized planetesimal with properties lying in the range of main belt asteroids. On the other hand, a transiting period significantly below 6 hr potentially indicates the existence of other physical processes (e.g., partial tidal disruption, collisions, gravitational instability) and/or a planetesimal with properties distinguishable from our understanding of rocky planetesimals. We acknowledge that the effect of ultimate tensile strength decays with the size of the body (Eq.12) such that a planetesimal with a smaller size can be circularized to a shorter orbital period without undergoing tidal disruption when other conditions remain identical. Furthermore, if the planetesimal is non-spherical, it undergoes tidal disruption at a larger distance compared to its spherical counterpart (see Appendix G).

4.3.1 The scale effect of ultimate tensile strength

The ultimate tensile strength potentially suffers from scale effect such that σ_s declines with the size of the body due to the increasing defects/cracks following the relation (Ahles et al. 2021):

$$\sigma_s \propto R^{-3\alpha_s}, \tag{14}$$

where α_s ranges from 0.1 to 0.7 (Popova et al. 2011). Compared to a cm-sized fragment of the planetesimal, there is at least a factor of ~ 100 reduction in the ultimate tensile strength for a planetesimal with $R_p = 100\,\mathrm{km}$. This reduction factor brings the hatched region corresponding to the properties of ordinary chondrites in Fig.10 to self-gravity dominant regime where $T_{min} \gtrsim 8\,\mathrm{hr}$.

We acknowledge that the declining trend in ultimate tensile strength with sample size remains uncertain, as the ultimate tensile strength may be more closely related to the composition, mineralogy and thermal history of the body, which vary a lot even within the same group of bodies (Pohl & Britt 2020), and are clearly dis-

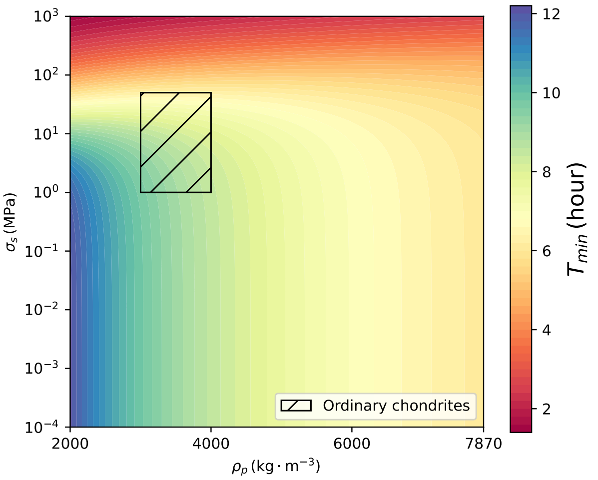

Figure 10. The minimum orbital period that a spherical and rigid planetesimal can circularize to without being tidally disrupted in ρ_p–σ_s space. Other system properties are listed in Table 3. The x-axes terminate at the density of iron and the hatched rectangle represents the estimated property range of ordinary chondrites (H chondirtes, L chondrites, and LL chondirtes) (Pohl & Britt 2020).

tinguished between the experimentally measured meteorite samples and planetesimals we consider in this study. We highlight the importance of this parameter for the results of this study, despite the large uncertainties of the value it would take in an exoplanetary system.

4.3.2 *Other potential scenarios*

In this study, we assume that the Roche limit corresponds to a hard cut-off, hence neglecting planetesimals scattered inside the Roche limit. In reality, tidal disruption of a planetesimal may take multiple orbits (Guillochon et al. 2011; Veras et al. 2017), especially when the planetesimal only enters its Roche limit briefly near the pericentre distance. For a realistic object, tidal disruption may also depend on the density gradient, chemical gradient and the rheology of the body (see Sridhar & Tremaine 1992 for an example of an object composed of viscous fluid).

There may exist a scenario where the planetesimal undergoes partial tidal disruption as well as tidal evolution. As the pseudo-synchronous spin rate decays (Fig.4, upper panel) and the pericentre distance increases with tidal evolution, the planetesimal migrates away from the shrinking Roche limit and tidal disruption ceases.

Meanwhile, thermal evolution of the planetesimal accompanied with tidal evolution may alter its shape, and the ultimate tensile strength, which potentially correlates with size, porosity, composition, mineralogy and thermal history (Pohl & Britt 2020), altering the Roche limit. The ultimate tensile strength may be correlated with the degree of deformation of the object (for instance, consider the correlation between ultimate tensile strength and Young's modulus). If σ_s is reduced and the planetesimal becomes more deformed (e.g., due to melting) during tidal evolution, the resultant increase in the Roche limit potentially re-triggers tidal disruption.

4.4 Comparison to the observed transiting systems

This work presents a model that predicts a population of planetesimals on a wide range of orbital periods around the white dwarf, potentially responsible for the observed transits. In this section, the single-body probability distribution obtained in Section 3.2 is expanded to a population of planetary systems, accounting for a variety of two-body system properties and tidal evolution stages, thus, mimicking the diversity of the chanced observations of transits. The predicted probability distribution is compared to the current observations in Fig.11 and summarized in Table 5.

To deduce the orbital parameters of a planetesimal around a white dwarf under tidal evolution, one need to know 1. the tidal evolution track of the planetesimal in a–e space (constrained by initial orbital parameters q_0 and Q_0) and 2. the position of the planetesimal on the tidal evolution tracks (the tidal evolution stage). Therefore, the corresponding minimum set of distributions required to account for the diversity of transiting systems is: 1. an initial orbital parameter distribution (q_0, Q_0) and 2. a tidal evolution stage distribution (multiple of tidal evolution time and tidal response, $T_p t$).

Fig.11 shows the orbital period distribution (left axis, histogram), together with a sampled eccentricity (black dots, right axis) and the cumulative distribution (black line, right axis). The normalised probability distribution is calculated by considering a uniform range of potential evolution times (from $t = 0$ to $t = 500$ Myr, with an interval of 5 Myr) and planetesimal densities ($\rho_p = 2000$–$8000\,\mathrm{kg \cdot m^{-3}}$ with an interval of $500\,\mathrm{kg \cdot m^{-3}}$). We assume that the ultimate tensile strength σ_s increases linearly with ρ_p from 1×10^5 Pa to 4×10^8 Pa (motivated by Ostrowski & Bryson 2019; Pohl & Britt 2020). The planetesimals are assumed to possess two Q_0, 3 AU and 5 AU with equal probability. Other parameters are identical to those listed in Table 3. Although our choices are arbitrary, one may expect that the predictions remain qualitatively similar for a range of free parameter distributions (see Section 4.2).

The observed transiting systems are generally consistent with our predictions: 1. more frequent short-period orbits plus a small enhancement towards longer period and 2. a higher probability towards the transition around the (nearly) circularized and partially circularized orbits. However, current observations are too few and do not form an unbiased distribution to compare with the simulated distribution. We note here that in reality, the probability of detecting a transiting planetesimal with a measured period may differ from the probability of having a planetesimal on such an orbital period (see Appendix F). Here we discuss each system individually.

4.4.1 *WD 1145+017*

The transiting planetesimal around WD 1145+017 is most likely in a circularized orbit, with a normalised probability of 1.8%. The 4.5 hr period is very close to the lower limit of the probability distribution. Within the context of this model, planetesimals are only circularized onto such a short-period orbit, if they undergo partial tidal disruption or possesses high ultimate tensile strength (Section 4.3). According to Fig.10 $\sigma_s \gtrsim 130$ MPa, which is of similar order of magnitude as the measured values for iron meteorites (Pohl & Britt 2020; Ahles et al. 2021), is required, if the planetesimal with $R_p = 100$ km is to avoid tidal disruption. Alternatively, if the planetesimal possess similar properties to ordinary chondritres, it must be smaller than ~ 50 km to avoid tidal disruption, well below the predicted value (Rappaport et al. 2016).

Interestingly, if the planetesimal orbiting WD 1145+0117 were to have the maximum ultimate tensile strength measured for meteorites, ~ 400 MPa (Ostrowski & Bryson 2019; Pohl & Britt 2020), the maximum radius of a planetesimal that would avoid tidal disruption is ~ 180 km, which is similar to the predicted size via the drift periods

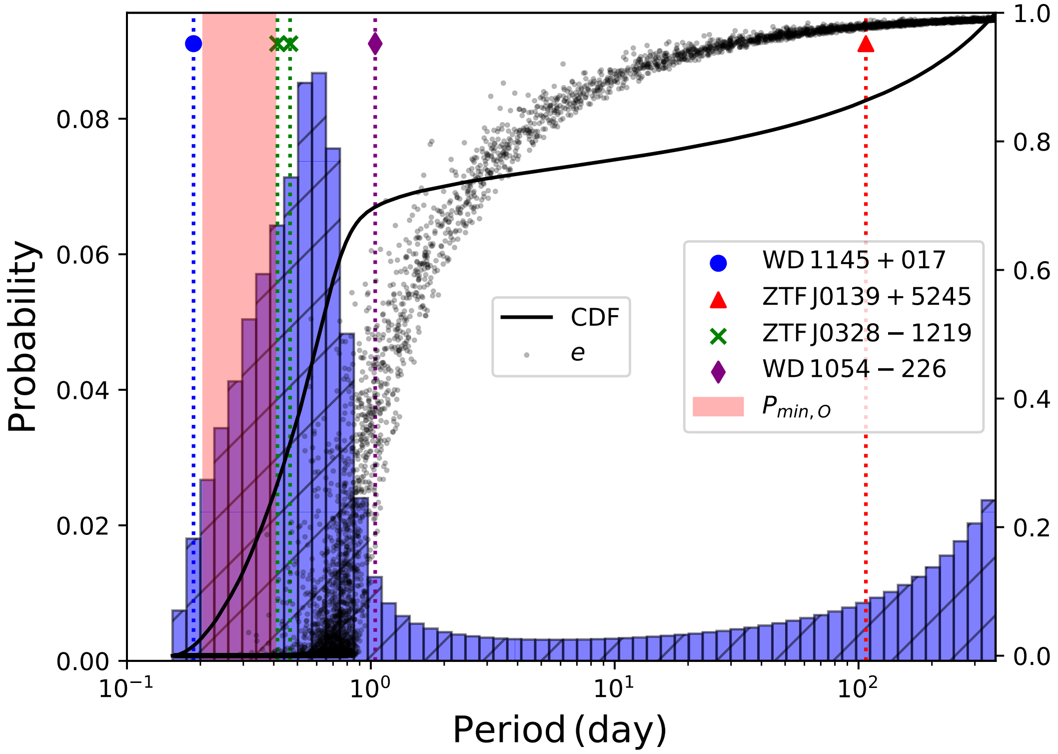

Figure 11. The probability distribution of orbital periods of a population of planetesimals, orbiting a population of white dwarfs under tidal evolution. Full details can be found in Section 4.4. Both the x-axis and the bin width are on the logarithmic scale. The black solid line is the cumulative distribution (right axis). The black dots are 10000 randomly sampled orbital eccentricities (right axis). The inferred period seen in the optical transits of WD 1145+017 (blue circle), ZTF J0139+5245 (red triangle), ZTF J0328-1219 (green crosses) and WD 1054–226 (purple diamond) are shown (Vanderburg et al. 2015; Vanderbosch et al. 2020, 2021; Farihi et al. 2022). The red shaded region is the range of minimum orbital period achievable by Solar System ordinary chondrites ($P_{min,O}$) as is predicted in Fig.10 (the hatched region).

System	Mass ($M_\odot$)	Cooling age (Myr)	Period	Predicted eccentricity	Predicted normalised probability (%)
WD 1145+017	0.6	175	4.5 hour	0	1.8
ZTF J0139+5245	0.52	-	107.2 day	~ 0.98	0.9
ZTF J0328-1219	0.73	1840	9.9 hour 11.2 hour	~ 0 ~ 0	6.4 7.1
WD 1054–226	0.62	1300	25 hour	~ 0.2–0.6	1.2

Table 5. A list of the properties of the observed transiting systems (Vanderburg et al. 2015; Vanderbosch et al. 2020, 2021; Farihi et al. 2022), together with the predicted orbital eccentricity and normalised (relative) probability (which, qualitative speaking, is insensitive to the number of bins of the histogram) based on the simulated distribution in Fig.11.

(Rappaport et al. 2016), potentially suggesting that the planetesimal already underwent partial tidal disruption.

We acknowledge that WD 1145+017 is an extreme of our model, with strict constraints on its properties (such an object may be quite rare, but not impossible, see e.g., Manser et al. 2019). Whilst this object can be explained in the context of the theory presented here, it does pose the question of why such an extreme case represents the first discovery of a white dwarf with optical transits. One possible explanation is the enhanced transit probability and signal-to-noise ratio towards smaller initial pericentre distance/smaller circularization period (Appendix F). Additionally, the exact tidal response of a body with the properties required to explain WD 1145+017, is not well understood and we acknowledge that some uncertainties remain in whether such a body can tidally circularize within the cooling age of WD 1145+017.

4.4.2 ZTF J0139+5245

The transiting period of ZTF J0139+5245 is best explained by a highly eccentric orbit with $e \sim 0.98$ and lies in the increasing trend of the predicted probability distribution towards long period, with a normalised probability of 0.9%. We postulate four reasons why long-period orbits may dominate this system (based on Section 4.2): 1. planetesimals are rarely scattered close to the white dwarf, 2.

planetesimals originate from close to the white dwarf (a close-in perturber due to e.g., planet-planet scattering or common envelope event), 3. planetesimals generally evolve slower under tides compared to our predictions, and 4. scattering takes longer (due to e.g., low mass perturbers).

4.4.3 ZTF J0328-1219

The transiting periods of ZTF J0328-1219 which most likely correspond to two (nearly) circularized orbits are close to the peak of the predicted probability distribution, with a normalised probability of 6.4% and 7.1%, respectively, corresponding to a combined probability of ∼ 9% of having two such planetesimals at the same time. As the peak of the distribution indicating the transition between (nearly) circularized orbits and partially circularized orbits shifts towards a longer orbital period with increasing $T_p t$ (3.2), the maximum probability of observing the two transiting periods around ZTF J0328-1219 is reached for a earlier tidal evolution stage: shorter tidal evolution time/weaker tidal response (8.8% and 8.5% for t = 0–100 Myr).

According to our model, properties of ordinary chonrites is sufficient for planetesimals to circularize onto the 9.9 hr and 11.2 hr orbits without undergoing tidal disruption, even when including scale effect and accounting for non-spherical bodies (see Appendix G).

4.4.4 WD 1054–226

The transiting period of WD 1054–226 most likely corresponds to a partially circularized orbit, whose eccentricity ranges from ∼ 0.2 to ∼ 0.6 according to our model, with a probability of 1.3%.

We cannot constrain the properties of planetesimals around ZTF J0139+5245 and WD 1054–226 as there is no direct relation between orbital period and initial pericentre distance for partially circularized orbits.

4.5 Implications

In this work, we study a potential evolution pathway of white dwarf planetary systems: planetesimals scattered barely outside the Roche limit undergoes tidal circularization (declining semi-major axis and eccentricity). This has crucial consequences for our view of planetary systems orbiting white dwarfs, with more objects potentially populating the inner regions closer to the white dwarf than previously thought. If these planetesimals control the periodic signals found in optical photometric monitoring of many white dwarfs, this scenario has testable observational consequences. Future observations should find a distribution of periods in the systems with optical transits that accumulates at both short-period (nearly) circularized orbits (∼ 10 hr), and at long-period highly eccentric orbits ($\gtrsim$ 100 day). This work highlights the importance of current and future observing facilities finding new candidate transiting systems, together with follow-up observations confirming their transiting periods. Those objects transiting with short periods that are likely on near-circular orbits has the following advantages:

- They provide the best potential tests for models of high eccentricity tidal migration.
- Their orbital period may help constrain where the tidally evolved planetesimals originate from and their properties.
- Practically, it is easier to constrain their orbital periods using dedicated high-speed photometric follow-up observing campaign in comparison to their long-period counterparts.

Optical transits around white dwarfs are only found in systems where planetary material has been accreted. Given the active dust production potentially required to produce the observed transit signatures, these systems provide an important clue in our understanding of how planetary material is accreted by white dwarfs. A better understanding of the evolution of white dwarf planetary systems will benefit the interpretation of planetary material accreted by white dwarfs that are used to probe the composition of exoplanetary bodies.

5 CONCLUSIONS

Planetary systems around white dwarfs are important targets to investigate the composition of exoplanetary systems. Transits of a handful of polluted white dwarfs provide key observational evidence regarding how planetary material is accreted. A number of mysteries remain regarding the exact details of the accretion process.

In this work, we investigate tidal circularization of planetesimals scattered close to white dwarfs exterior to the Roche limit. Tidally evolved planetesimals are predicted to exist on a wide range of orbital periods, potentially linked to the photometric variability of a handful of polluted white dwarfs, with the orbital periods of the planetesimals controlling the periodic signals seen in the optical data.

Our simulations predict that under tidal evolution, there exists a population of planetesimals on short-period (nearly) circularized orbits around white dwarfs (peaking at ∼ 10 hour–1 day), potentially represented by systems such as WD 1145+017, ZTF J0328-1219 and WD 1054–226. Alongside these, there is a population of planetesimals on long-period highly eccentric orbits (∼ 100 day) such as seen for ZTF J0139+5245 exist, together with a low probability of finding planetesimlas on orbital periods of ∼ 1 day–100 day.

While the orbital periods of most transiting systems can be explained by tidally evolved planetesimals with properties similar to Solar System ordinary chondrites, in order to avoid tidal disruption, the planetesimal on the 4.5 hour period around WD 1145+017 must possess an ultimate tensile strength of the same order of magnitude as iron meteorites.

Currently, this field is limited by the small number of transiting systems characterised so far. Whilst the current observations are inline with the theory presented here, the true test will be comparison of the prediction orbital distribution with the results of the many current and future optical photometric monitoring surveys, including ZTF and Roman Observatories.

ACKNOWLEDGEMENTS

We would like to thank Dimitri Veras, Siyi Xu and Zach Vanderbosch for valuable discussions regarding various aspects of this paper. AB and LKR acknowledges the support of a Royal Society University Research Fellowship, URF\R1\211421. YL acknowledges the support of a STFC studentship. LKR acknowledges support of an ESA Co-Sponsored Research Agreement No. 4000138341/22/NL/GLC/my = Tracing the Geology of Exoplanets

DATA AVAILABILITY

Codes and data used in this work are available upon reasonable request to the author, Yuqi Li.

REFERENCES

Ahles A. A., Emery J. D., Dunand D. C., 2021, Acta Astronautica, 189, 465

Bagheri A., et al., 2022, Advances in Geophysics, 63, 231

Barnes R., 2017, Celestial Mechanics and Dynamical Astronomy, 129, 509

Bear E., Soker N., 2015, MNRAS, 450, 4233

Beaugé C., Nesvorný D., 2012, ApJ, 751, 119

Becker J., Seligman D. Z., Adams F. C., Styczinski M. J., 2023, ApJ, 945, L24

Becklin E. E., Farihi J., Jura M., Song I., Weinberger A. J., Zuckerman B., 2005, ApJ, 632, L119

Bellm E. C., et al., 2019, PASP, 131, 018002

Beuthe M., 2013, Icarus, 223, 308

Bolmont E., Raymond S. N., Leconte J., 2011, A&A, 535, A94

Bonsor A., Mustill A. J., Wyatt M. C., 2011, MNRAS, 414, 930

Bonsor A., Augereau J. C., Thébault P., 2012, A&A, 548, A104

Bonsor A., Farihi J., Wyatt M. C., van Lieshout R., 2017, MNRAS, 468, 154

Borucki W. J., et al., 2010, Science, 327, 977

Boué G., Efroimsky M., 2019, Celestial Mechanics and Dynamical Astronomy, 131, 30

Brouwers M. G., Bonsor A., Malamud U., 2022, MNRAS, 509, 2404

Brown J. C., Veras D., Gänsicke B. T., 2017, MNRAS, 468, 1575

Choi J., Dotter A., Conroy C., Cantiello M., Paxton B., Johnson B. D., 2016, ApJ, 823, 102

Clausen N., Tilgner A., 2015, A&A, 584, A60

Croll B., et al., 2017, ApJ, 836, 82

Davidsson B. J. R., 1999, Icarus, 142, 525

Davies A. G., Perry J. E., Williams D. A., Nelson D. M., 2024, Nature Astronomy, 8, 94

Debes J. H., Kilic M., Faedi F., Shkolnik E. L., Lopez-Morales M., Weinberger A. J., Slesnick C., West R. G., 2012, ApJ, 754, 59

Dong J., et al., 2021, ApJ, 920, L16

Dotter A., 2016, ApJS, 222, 8

Downey B. G., Nimmo F., Matsuyama I., 2023, Icarus, 389, 115257

Duvvuri G. M., Redfield S., Veras D., 2020, ApJ, 893, 166

Farhat M., Auclair-Desrotour P., Boué G., Laskar J., 2022, A&A, 665, L1

Farihi J., 2016, New Astron. Rev., 71, 9

Farihi J., Jura M., Zuckerman B., 2009, ApJ, 694, 805

Farihi J., Jura M., Lee J. E., Zuckerman B., 2010, ApJ, 714, 1386

Farihi J., et al., 2022, MNRAS, 511, 1647

Gaia Collaboration et al., 2016, A&A, 595, A1

Gänsicke B. T., Marsh T. R., Southworth J., 2007, MNRAS, 380, L35

Gänsicke B. T., et al., 2016, ApJ, 818, L7

Gary B. L., Rappaport S., Kaye T. G., Alonso R., Hambschs F. J., 2017, MNRAS, 465, 3267

Glanz H., Rozner M., Perets H. B., Grishin E., 2022, ApJ, 931, 11

Goldreich P., 1966, Reviews of Geophysics and Space Physics, 4, 411

Guidry J. A., et al., 2021, ApJ, 912, 125

Guillochon J., Ramirez-Ruiz E., Lin D., 2011, ApJ, 732, 74

Hansen B. M. S., 2012, ApJ, 757, 6

Heller R., Leconte J., Barnes R., 2011, A&A, 528, A27

Howell S. B., et al., 2014, PASP, 126, 398

Hut P., 1981, A&A, 99, 126

Ibgui L., Burrows A., Spiegel D. S., 2010, ApJ, 713, 751

Ivezić Ž., et al., 2019, ApJ, 873, 111

Jura M., Farihi J., Zuckerman B., 2007, ApJ, 663, 1285

Jura M., Farihi J., Zuckerman B., 2009, AJ, 137, 3191

Kagan B. A., 1997, Progress in Oceanography, 40, 109

Kawahara H., Hirano T., Kurosaki K., Ito Y., Ikoma M., 2013, ApJ, 776, L6

Kepler S. O., Kleinman S. J., Nitta A., Koester D., Castanheira B. G., Giovannini O., Costa A. F. M., Althaus L., 2007, MNRAS, 375, 1315

Kepler S. O., Koester D., Romero A. D., Ourique G., Pelisoli I., 2017, in Tremblay P. E., Gaensicke B., Marsh T., eds, Astronomical Society of the Pacific Conference Series Vol. 509, 20th European White Dwarf Workshop. p. 421 (`arXiv:1610.00371`), doi:10.48550/arXiv.1610.00371

Kervazo M., Tobie G., Choblet G., Dumoulin C., Běhounková M., 2022, Icarus, 373, 114737

Kilic M., von Hippel T., Leggett S. K., Winget D. E., 2005, ApJ, 632, L115

Kilic M., von Hippel T., Leggett S. K., Winget D. E., 2006, ApJ, 646, 474

Koester D., Gänsicke B. T., Farihi J., 2014, A&A, 566, A34

Lai S., et al., 2021, ApJ, 920, 156

Lambeck K., 1977, Philosophical Transactions of the Royal Society of London Series A, 287, 545

Leconte J., Chabrier G., Baraffe I., Levrard B., 2010, A&A, 516, A64

Levrard B., Correia A. C. M., Chabrier G., Baraffe I., Selsis F., Laskar J., 2007, A&A, 462, L5

Lu T., Rein H., Tamayo D., Hadden S., Mardling R., Millholland S. C., Laughlin G., 2023, ApJ, 948, 41

Makarov V. V., Efroimsky M., 2013, ApJ, 764, 27

Manser C. J., et al., 2019, Science, 364, 66

Manser C. J., et al., 2024, MNRAS, 531, L27

Matsumura S., Peale S. J., Rasio F. A., 2010, ApJ, 725, 1995

Melis C., Jura M., Albert L., Klein B., Zuckerman B., 2010, ApJ, 722, 1078

Miller N., Fortney J. J., Jackson B., 2009, ApJ, 702, 1413

Moe M., Kratter K. M., 2018, ApJ, 854, 44

Mustill A. J., Villaver E., Veras D., Gänsicke B. T., Bonsor A., 2018, MNRAS, 476, 3939

Nedelcu D. A., Birlan M., Popescu M., Bădescu O., Pricopi D., 2014, A&A, 567, L7

Neron de Surgy O., Laskar J., 1997, A&A, 318, 975

Nesvorný D., Vokrouhlický D., Morbidelli A., Bottke W. F., 2009, Icarus, 200, 698

Noyelles B., Frouard J., Makarov V. V., Efroimsky M., 2014, Icarus, 241, 26

O'Brien M. W., et al., 2023, MNRAS, 518, 3055

O'Brien M. W., et al., 2024, MNRAS, 527, 8687

O'Connor C. E., Lai D., 2020, MNRAS, 498, 4005

O'Connor C. E., Teyssandier J., Lai D., 2022, MNRAS, 513, 4178

Ostrowski D., Bryson K., 2019, Planet. Space Sci., 165, 148

Pohl L., Britt D. T., 2020, Meteoritics & Planetary Science, 55, 962

Popova O., Borovička J., Hartmann W. K., Spurný P., Gnos E., Nemtchinov I., Trigo-Rodríguez J. M., 2011, Meteoritics & Planetary Science, 46, 1525

Press W. H., Teukolsky S. A., 1977, ApJ, 213, 183

Rappaport S., Barclay T., DeVore J., Rowe J., Sanchis-Ojeda R., Still M., 2014, ApJ, 784, 40

Rappaport S., Gary B. L., Kaye T., Vanderburg A., Croll B., Benni P., Foote J., 2016, MNRAS, 458, 3904

Rathbun J. A., Lopes R. M. C., Spencer J. R., 2018, AJ, 156, 207

Ricker G. R., et al., 2014, in Oschmann Jacobus M. J., Clampin M., Fazio G. G., MacEwen H. A., eds, Society of Photo-Optical Instrumentation Engineers (SPIE) Conference Series Vol. 9143, Space Telescopes and Instrumentation 2014: Optical, Infrared, and Millimeter Wave. p. 914320 (`arXiv:1406.0151`), doi:10.1117/12.2063489

Rodet L., Lai D., 2024, MNRAS, 527, 11664

Rozner M., Glanz H., Perets H. B., Grishin E., 2022, ApJ, 931, 10

Rufu R., Canup R. M., 2020, Journal of Geophysical Research (Planets), 125, e06312

Sánchez M. B., de Elía G. C., Downes J. J., 2020, A&A, 637, A78

Sanchis-Ojeda R., et al., 2015, ApJ, 812, 112

Seligman D. Z., et al., 2024, ApJ, 961, 22

Sridhar S., Tremaine S., 1992, Icarus, 95, 86

Storch N. I., Lai D., 2014, MNRAS, 438, 1526

Tobie G., Mocquet A., Sotin C., 2005, Icarus, 177, 534

Tremblay P. E., Cummings J., Kalirai J. S., Gänsicke B. T., Gentile-Fusillo N., Raddi R., 2016, MNRAS, 461, 2100

Tyler R. H., 2021, The Planetary Science Journal, 2, 70

Tyler R. H., Henning W. G., Hamilton C. W., 2015, ApJS, 218, 22

Vanderbosch Z., et al., 2020, ApJ, 897, 171

Vanderbosch Z. P., et al., 2021, ApJ, 917, 41

Vanderburg A., et al., 2015, Nature, 526, 546

Veras D., 2016, Royal Society Open Science, 3, 150571

Veras D., Fuller J., 2019, MNRAS, 489, 2941

Veras D., Fuller J., 2020, MNRAS, 492, 6059

Veras D., Carter P. J., Leinhardt Z. M., Gänsicke B. T., 2017, MNRAS, 465, 1008

Veras D., et al., 2019, MNRAS, 486, 3831

Veras D., Georgakarakos N., Mustill A. J., Malamud U., Cunningham T., Dobbs-Dixon I., 2021, MNRAS, 506, 1148
Veras D., Georgakarakos N., Dobbs-Dixon I., 2023, MNRAS, 518, 4537
Veras D., Mustill A. J., Bonsor A., 2024, Reviews in Mineralogy and Geochemistry, 90, 141
Vick M., Lai D., 2020, MNRAS, 496, 3767
Vick M., Lai D., Anderson K. R., 2019, MNRAS, 484, 5645
Vick M., Su Y., Lai D., 2023, ApJ, 943, L13
Wang L., Zhang X., Wang J., Zhang Z.-X., Fang T., Gu W.-M., Guo J., Jiang X., 2023, ApJ, 944, 23
Willems B., Deloye C. J., Kalogera V., 2010, ApJ, 713, 239
Wilson T. G., Farihi J., Gänsicke B. T., Swan A., 2019, MNRAS, 487, 133
Xu S., Jura M., Pantoja B., Klein B., Zuckerman B., Su K. Y. L., Meng H. Y. A., 2015, ApJ, 806, L5
Xu S., Lai S., Dennihy E., 2020, ApJ, 902, 127
Zahnle K. J., Lupu R., Dobrovolskis A., Sleep N. H., 2015, Earth and Planetary Science Letters, 427, 74
Zuckerman B., Becklin E. E., 1987, Nature, 330, 138
Zuckerman B., Koester D., Reid I. N., Hünsch M., 2003, ApJ, 596, 477
Zuckerman B., Melis C., Klein B., Koester D., Jura M., 2010, ApJ, 722, 725
van Lieshout R., Min M., Dominik C., 2014, A&A, 572, A76
van Lieshout R., et al., 2016, A&A, 596, A32

This paper has been typeset from a TEX/LATEX file prepared by the author.

Appendices

Yuqi Li

June 26, 2025

A Simplified tidal evolution equations

In order to illustrate the properties of the CTL model (Hut, 1981; Levrard et al., 2007; Leconte et al., 2010; Matsumura et al., 2010; Bolmont et al., 2011; Heller et al., 2011; Beaugé & Nesvorný, 2012; Hansen, 2012; Glanz et al., 2022; Rozner et al., 2022; Lu et al., 2023) more clearly, we simplify the coupled tidal evolution equations based on the fact that the orbital angular momentum of a white dwarf-planetesimal system is conserved:

$$a(1-e^2) = \frac{2q_0Q_0}{q_0+Q_0}, \tag{A1}$$

and the fact that the planetesimal reaches pseudo-synchronization and spin-orbit (mis)alignment rapidly. In this case the coupled tidal evolution equations are simplified to:

$$\frac{de}{dt} = 9GT_pO_{-8}F_e(e), \tag{A2}$$

$$\frac{da}{dt} = 2GT_pO_{-7}F_a(e), \tag{A3}$$

$$\omega_{eq} = \left[G(M_p+M_*)\right]^{\frac{1}{2}}\left(\frac{q_0+Q_0}{2q_0Q_0}\right)^{\frac{3}{2}}\frac{f_2(e)}{f_5(e)}, \tag{A4}$$

$$\epsilon_p = \begin{cases} 0 & 0 \le \epsilon_{p,0} < \frac{\pi}{2} \\ \pi & \frac{\pi}{2} < \epsilon_{p,0} \le \pi \end{cases}, \tag{A5}$$

where T_p, O_l $F_e(e)$ and $F_a(e)$ are given by:

$$T_p \equiv \frac{K_p(M_p+M_*)M_*R_p^5}{M_p} \approx \frac{K_pM_*^2R_p^5}{M_p} \propto \frac{K_pM_*^2R_p^2}{\rho_p}, \tag{A6}$$

$$O_l \equiv \left(\frac{2q_0Q_0}{q_0+Q_0}\right)^l, \tag{A7}$$

$$F_e(e) = e(1-e^2)^{\frac{3}{2}}\left[\frac{11}{18}\frac{f_2(e)f_4(e)}{f_5(e)} - f_3(e)\right], \tag{A8}$$

$$F_a(e) = (1-e^2)^{-\frac{1}{2}}\left[\frac{f_2^2(e)}{f_5(e)} - f_1(e)\right]. \tag{A9}$$

We can deduce the following properties of the CTL model:

- Tidal evolution track in a–e space is determined by $F_e(e)/F_a(e)$, which means that it is fixed for a given set of (q_0, Q_0).
- Tidal evolution rates in both a and e are scaled by T_p, such that for a fixed (q_0, Q_0), T_pt determines the tidal evolution stage (tidal evolution is simultaneous in T_pt space).
- At identical e and for $q_0 \ll Q_0$, O_l indicates that a planetesimal starts at a smaller q_0 evolves much faster.
- $\frac{de}{dt} \propto F_e(e) \leq 0$ has its minimum at $e \approx 0.658$, converging to 0 at both $e \longrightarrow 0$ and $e \longrightarrow 1$,
- $\frac{da}{dt} \propto F_a(e) \leq 0$ decreases monotonically with e, converging to 0 at $e \longrightarrow 0$.
- $\frac{dT}{dt} \propto a^{\frac{1}{2}}\frac{da}{dt} \propto (1-e^2)^{-\frac{1}{2}}F_a(e) \leq 0$ has the same qualitative behaviour as $F_a(e)$ while decreasing more strongly with e.
- Pseudo-synchronous spin rate of the planetesimal decreases along the tidal evolution track.

B Analytical tidal circularization timescale

One can approximate the circularization timescale by analyzing $|\frac{\dot{a}}{a}|_0$ in the limit of $q_0 \ll Q_0$ ($e_0 = \frac{2Q_0}{q_0+Q_0} - 1 \longrightarrow 1$). We expand the terms in the square brackets in Eq.A9 at $e_0 = 1$ such that:

$$\left[\frac{f_2^2(e_0)}{f_5(e_0)} - f_1(e_0)\right] \approx -\frac{4059}{320} - \frac{264(e_0-1)}{5}. \tag{B1}$$

We then expand at $\frac{q_0}{Q_0} = 0$ and get:

$$
\begin{aligned}
\left|\frac{\dot{a}}{a}\right|_0 &\approx 2GT_p\left(\frac{2q_0Q_0}{q_0+Q_0}\right)^{-8}(1-e_0^2)^{\frac{1}{2}}\left[\frac{4059}{320}-\frac{264(1-e_0)}{5}\right]\\
&\approx 2GT_p\frac{4059}{320}\left(2q_0\right)^{-8}\left(4\frac{q_0}{Q_0}\right)^{\frac{1}{2}}\\
&\approx 0.2GT_pq_0^{-7.5}Q_0^{-0.5},
\end{aligned}
\tag{B2}
$$

such that $\tau_{cir} \approx \frac{5}{GT_p}q_0^{7.5}Q_0^{0.5}$, increasing much more rapidly with q_0 than Q_0 and T_p.

C Interpretations of orbital period distribution

In this section we focus on the case where $e \longrightarrow 0$ and $q_0 \ll Q_0$. We will use the fact that on the logarithmic scale, the widths of the bins of the orbital period distribution histogram ΔT satisfies $\frac{\Delta T}{T}$ = constant, while on the linear scale, ΔT is a constant.

Eq.A1 implies:

$$
2\Delta q_0 = (a+\Delta a)[1-(e+\Delta e)^2] - a(1-e^2),
\tag{C1}
$$

where $\Delta a = a(q_0+\Delta q_0) - a(q_0)$, and $\Delta e = e(q_0+\Delta q_0) - e(q_0)$.

Kepler's third law implies that:

$$
\begin{aligned}
&a = AT^{\frac{2}{3}},\\
&\frac{\Delta a}{a} = (1+\frac{\Delta T}{T})^{\frac{2}{3}} - 1,
\end{aligned}
\tag{C2}
$$

where A is a positive proportionality constant.

Eq.C1 and Eq.C2 combine to give:

$$
2\Delta q_0 = a(1+\frac{\Delta T}{T})^{\frac{2}{3}}[1-(e+\Delta e)^2] - a(1-e^2),
\tag{C3}
$$

where $\Delta q_0 = q_0(T+\Delta T) - q_0(T)$ (for the orbital period distribution histogram, ΔT is the bin width and T is its inner bin edge). By substituting $a(1-e^2) = 2q_0$, Eq.C3 can be expressed as:

$$
\frac{\Delta q_0}{q_0} = (1+\frac{\Delta T}{T})^{\frac{2}{3}}\left[\frac{1-(e+\Delta e)^2}{1-e^2}\right] - 1.
\tag{C4}
$$

After applying the PDF $P(q_0) \propto q_0^{\alpha}$, one can write (for $\alpha \neq -1$):

$$\begin{aligned} P([T, T+\Delta T]) &= P([q_0, q_0+\Delta q_0]) \\ &= \int_{q_0}^{q_0+\Delta q_0} P(q_0')dq_0' \\ &= N_\alpha \left[(q_0+\Delta q_0)^{\alpha+1} - q_0^{\alpha+1}\right] \\ &= N_\alpha q_0^{\alpha+1} \left| \left(1+\frac{\Delta T}{T}\right)^{\frac{2}{3}\alpha+\frac{2}{3}} \left[\frac{1-(e+\Delta e)^2}{1-e^2}\right]^{\alpha+1} - 1 \right| \\ &= N_\alpha \left(\frac{A}{2}\right)^{\alpha+1} T^{\frac{2}{3}\alpha+\frac{2}{3}} \times \\ & \left| \left(1+\frac{\Delta T}{T}\right)^{\frac{2}{3}\alpha+\frac{2}{3}} \left[1-(e+\Delta e)^2\right]^{\alpha+1} - (1-e^2)^{\alpha+1} \right|, \end{aligned} \tag{C5}$$

where N_α is a positive normalisation constant for α. When $\alpha > -1$, the absolute value signs in Eq.C5 can be omitted. A positive α is usually expected as it is less likely for a planetesimal to be scattered to a smaller pericentre distance (Rodet & Lai, 2024) but we will discuss the case where $\alpha < 0$ for completeness.

For $\alpha = -1$, we have:

$$\begin{aligned} P([T, T+\Delta T]) &= P([q_0, q_0+\Delta q_0]) \\ &= N_{-1} \left[\ln{(q_0+\Delta q_0)} - \ln{q_0}\right] \\ &= N_{-1} \ln\left(1+\frac{\Delta q_0}{q_0}\right) \\ &= N_{-1} \ln\left\{\left(1+\frac{\Delta T}{T}\right)^{\frac{2}{3}} \left[\frac{1-(e+\Delta e)^2}{1-e^2}\right]\right\}. \end{aligned} \tag{C6}$$

For (nearly) circularized orbits ($e \longrightarrow 0$, $\Delta e \longrightarrow 0$, $a = 2q_0$), we have, for $\alpha \neq -1$:

$$P([T, T+\Delta T] | e \longrightarrow 0) = N_\alpha \left(\frac{A}{2}\right)^{\alpha+1} T^{\frac{2}{3}\alpha+\frac{2}{3}} \left| \left(1+\frac{\Delta T}{T}\right)^{\frac{2}{3}\alpha+\frac{2}{3}} - 1 \right|, \tag{C7}$$

where a special point is $\alpha = \frac{1}{2}$ (the fiducial value used in the main text), such that:

$$P([T, T+\Delta T] | e \longrightarrow 0) = N_{\frac{1}{2}} \left(\frac{A}{2}\right)^{\frac{3}{2}} \Delta T, \tag{C8}$$

which returns a uniform distribution on the linear scale where $\Delta T =$ constant (see the zoom-in plot of Fig.6 in the main text). Meanwhile, on the logarithmic scale where $\frac{\Delta T}{T} =$ constant, we have:

$$P([T, T+\Delta T] | e \longrightarrow 0) = B T^{\frac{2}{3}\alpha+\frac{2}{3}}, \tag{C9}$$

where $B = N_\alpha \left(\frac{A}{2}\right)^{\alpha+1} \left|\left(1+\frac{\Delta T}{T}\right)^{\frac{2}{3}\alpha+\frac{2}{3}} - 1\right|$ is a constant. For $\alpha = \frac{1}{2}$, the probability distribution is linearly proportional to T for (nearly) circularized orbits, consistent with Fig.6 in the main text.

For $\alpha = -1$, we have:

$$P([T, T+\Delta T]|e \to 0) = \frac{2}{3} N_{-1} \ln\left(1+\frac{\Delta T}{T}\right), \tag{C10}$$

which returns a uniform distribution on the logarithmic scale where $\frac{\Delta T}{T}$ = constant (see the lower-right panel of Fig.8 in the main text where the CDF is linear on the logarithmic scale).

The analysis above indicates that the probability distribution of the period for (nearly) circularized orbits help probe the initial pericentre distance distribution. This is expected as a (and hence T) is directly related to q_0 for (nearly) circularized orbits.

On the other hand, the probability distribution for non-zero eccentricity is not straightforward. We provide a conceptual interpretation here. Imagine two planetesimals starting at identical Q_0 but different q_0 with $q_0 \ll Q_0$, such that they possess similar initial semi-major axis and initial orbital period. Then, when we start the tidal evolution, Eq.B2 implies that the a and T of the planetesimal starts at a smaller q_0 decays much faster. Therefore, the difference in T of these two planetesimals increase, such that these two planetesimals become more loosely packed in period space. Now, consider a second scenario where the planetesimal starting at a smaller q_0 is nearly circularized, such that its $|\frac{dT}{dt}|$ converges to 0, while its counterpart is still on a partially circularized orbit. In this scenario, as T of the planetesimal with a larger q_0 continues to decrease towards its minimum (which is larger than its counterpart), the difference in T of these two planetesimals declines and these two planetesimals become more closely packed in period space. The decay of the difference in T continues until the planetesimal starting at a larger q_0 is (nearly) circularized, where these two planetesimals are in the most closely packed state (see the lower panel of Fig.4 in the main text). To sum up, tidal circularization looses the packing of orbits in period space at an early tidal evolution stage and then tightens the packing towards short-period (nearly) circularized orbits. Hence, planetesimals tend to pile up towards short-period (nearly) circularized orbits and long-period highly eccentric orbits. These scenarios are shown in Fig.4 and Fig.7 in the main text. In Fig.4, the orbital period difference of two planetesimals starting at different q_0 initially increases and then decays during tidal evolution, reaching a constant after both planetesimals are circularized. In Fig.7, the initially closely packed orbits in period space at $t = 0$ looses between $T \sim 1$ day and $T \sim 100$ day. Towards $T \lesssim 1$ day, the nearly circularized orbits become more closely packed where a given ΔT covers a larger Δq_0. These features are consistent with the obtained orbital period distribution in Fig.6 in the main text.

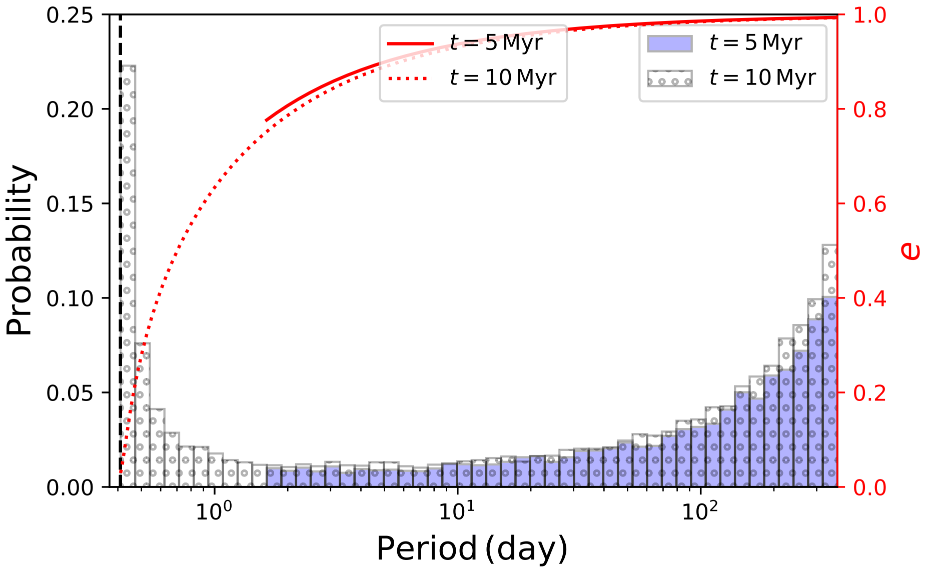

Figure D1: Same plot as Fig.6 in the main text, but for shorter tidal evolution timescales, $t = 5\,\mathrm{Myr}$ and $t = 10\,\mathrm{Myr}$. The distribution is normalised with respect to $t = 5\,\mathrm{Myr}$.

D Orbital period distribution at an early tidal evolution phase

In Fig.D1 and Fig.D2, we plot the short tidal evolution time/weaker tidal response (note that t and T_p are degenerate such that tidal evolution is simultaneous in $T_p t$ space) counterparts to Fig.6 and the upper-left panel of Fig.8 in the main text. In Fig.D1, one can see that the peak towards short period is not present at a tidal evolution time of 5 Myr, where the minimum eccentricity is around 0.8. At a tidal evolution time of 10 Myr, the peak appears as the minimum eccentricity approaches 0. Similarly, in Fig.D2, the CDF truncates before the minimum orbital period (dashed line) for a tidal evolution time of 6 Myr and 7 Myr. However, at a tidal evolution time of 7 Myr, there already exists a small peak (see the gradient of the CDF) towards the shortest orbital period.

E Cumulative distribution of orbital period for different forms of initial pericentre distribution

In Fig.E1, we plot the resultant orbital period distribution for different forms of probability density function of q_0. The qualitative features: a peak at the short-period nearly circularized orbits ($\sim$ 10 hr–1 day) and the increasing tail towards long-period highly eccentric orbits ($\sim$ 100 day) on the logarithmic scale persists.

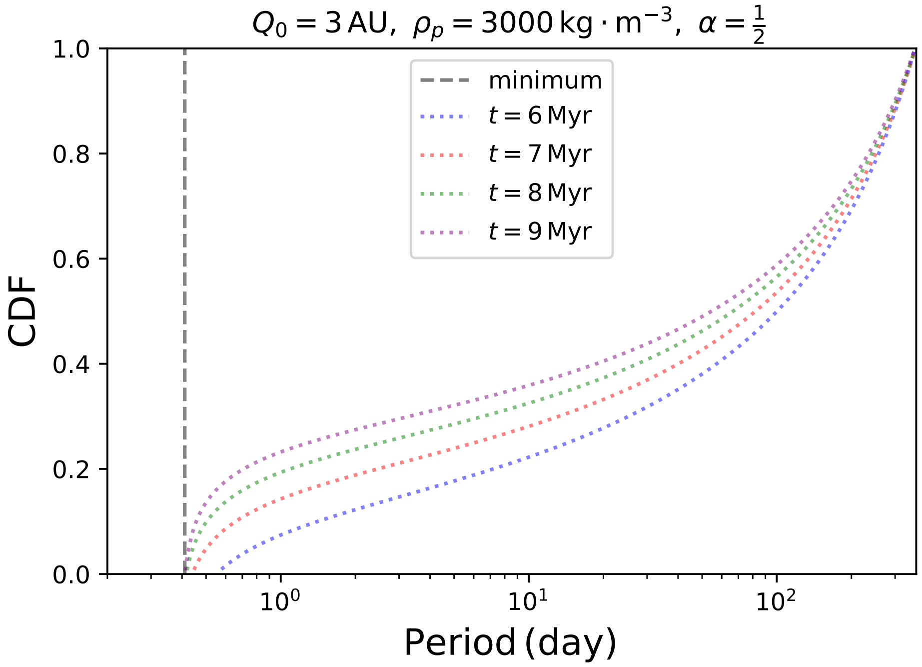

Figure D2: Same plot as the upper-left panel of Fig.9 in the main text, but for shorter tidal evolution timescales.

F Observational probability

The transit probability of a planetesimal can be expressed as (Barnes, 2007):

$$P_{transit} = \frac{R_* + R_{eff}}{a(1-e^2)}, \tag{F1}$$

where R_{eff} is the maximum extent of the planetesimal in the direction perpendicular to the orbital plane that is optically thick. By using Eq.A1, one can write:

$$P_{transit} = \frac{(R_* + R_{eff})(q_0 + Q_0)}{2q_0Q_0}, \tag{F2}$$

which decreases with the increase in q_0.

The transit duration of a planetesimal can be expressed as (Tingley & Sackett, 2005; Burke, 2008):

$$\tau_{transit} = \frac{2(R_* + R_{eff})r}{\sqrt{G(M_* + M_p)a(1-e^2)}}\sqrt{1 - \frac{r^2\cos^2 i}{(R_* + R_{eff})^2}}, \tag{F3}$$

where R_{eff} depends on the shape, extent of the optically thick region and the orbital inclination i, $r = \frac{a(1-e^2)}{1+e\cos f}$ is the distance of the planetesimal from the white dwarf with f the true anomaly.

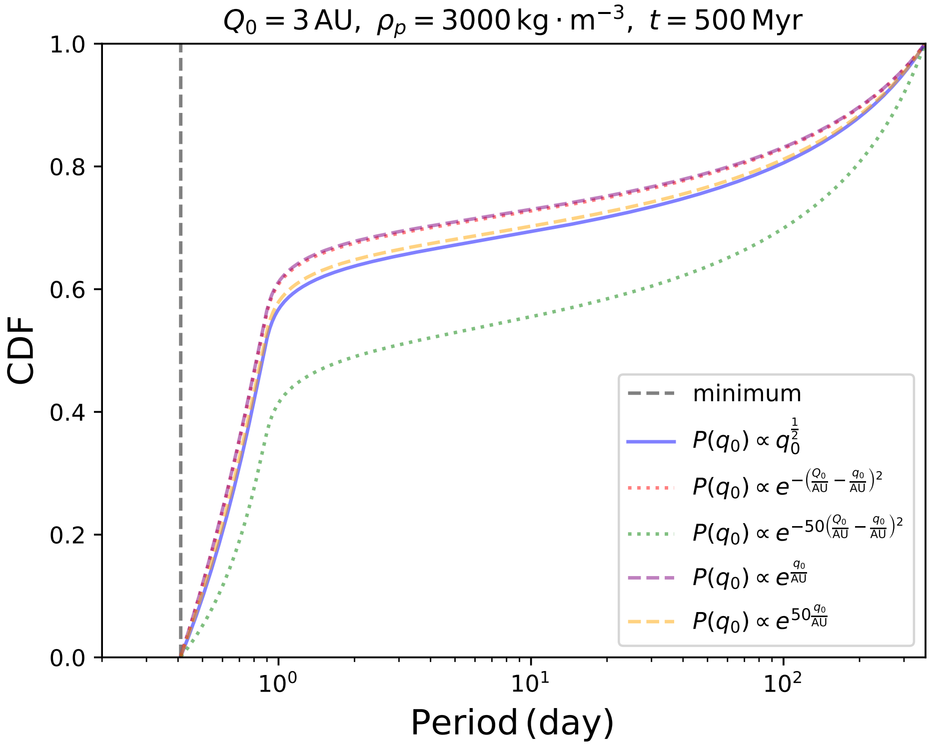

Figure E1: The cumulative distribution of planetesimal's period within 1 year for different forms of initial pericentre distribution.

For a random viewing angle, it is more natural to compute the spatial (uniformly distributed true anomaly) or temporal average (a $f(t)$ distribution with t uniformly distributed between 0 and orbital period) of Eq.F3. In the limit of $i \to 90°$, where R_{eff} represents the maximum extent of the planetesimal in the orbital direction that is optically thick, the averaged Eq.F3 is:

$$\begin{aligned} < \tau_{transit} >_{spatial} &= \frac{2(R_* + R_{eff})}{\sqrt{G(M_* + M_p)a(1-e^2)}} \frac{1}{2\pi} \int_0^{2\pi} r df \\ &= \frac{2(R_* + R_{eff})a\sqrt{1-e^2}}{\sqrt{G(M_* + M_p)a(1-e^2)}} \\ &= \frac{2(R_* + R_{eff})a^{\frac{1}{2}}}{\sqrt{G(M_* + M_p)}} \propto a^{\frac{1}{2}}, \end{aligned} \tag{F4}$$

$$\begin{aligned} < \tau_{transit} >_{time} &= \frac{2(R_* + R_{eff})}{\sqrt{G(M_* + M_p)a(1-e^2)}} \frac{1}{T} \int_0^{T} r dt \\ &= \frac{2(R_* + R_{eff})a(1+\frac{e^2}{2})}{\sqrt{G(M_* + M_p)a(1-e^2)}} \\ &\propto a^{\frac{1}{2}}(1+\frac{e^2}{2})(1-e^2)^{-\frac{1}{2}}. \end{aligned} \tag{F5}$$

The transit duration is closely correlated with the signal-to-noise ratio (von Braun et al., 2009):

$$\mathrm{SNR} = \sqrt{\frac{(d_{transit}N_{transit})^2}{\sum_i \left[N_i^2(\frac{\sigma_w^2}{N_i} + \sigma_r^2)\right]}}, \tag{F6}$$

where $d_{transit}$ is the transit depth, $N_{transit}$ is the total number of data points collected during all the transits, N_i is the number of data points collected during the ith transit, such that $\sum_i N_i = N_{transit}$, with i ranging from 1 to the nearest integer of $\frac{\tau_{obs}}{T}$, σ_w and σ_r represents white noise and red noise. Assuming identical observational conditions, we have $N_{transit} \propto \frac{\tau_{transit}}{T}$ and $N_i \propto \tau_{transit}$, $\sum_i N_i^2 \propto \frac{\tau_{transit}^2}{T}$.

We investigate the SNR in two limiting cases. In the white noise dominant limit:

$$\mathrm{SNR}_w \propto \sqrt{N_{transit}} \propto \sqrt{\frac{\tau_{transit}}{T}} \propto \sqrt{\tau_{transit}}a^{-\frac{3}{4}}, \tag{F7}$$

which can be expressed in a and e by substituting Eq.F4 or Eq.F5.

In terms of the spatial average, the SNR in the white noise dominant limit is:

$$\mathrm{SNR}_{w,s} \propto a^{-\frac{1}{2}}. \tag{F8}$$

In terms of the time average, the SNR can be expressed as:

$$\begin{aligned}\mathrm{SNR}_{w,t} &\propto a^{-\frac{1}{2}}(1+\frac{e^2}{2})^{\frac{1}{2}}(1-e^2)^{-\frac{1}{4}} \\ &\propto \left(\frac{q_0+Q_0}{2q_0Q_0}\right)^{\frac{1}{2}}\left(-\frac{e^6}{4}-\frac{3e^4}{4}+1\right)^{\frac{1}{4}},\end{aligned} \tag{F9}$$

which increases with the decreasing initial pericentre distance and decreasing orbital eccentricity.

In the red noise dominant limit, the SNR is independent of the transit duration:

$$\mathrm{SNR}_r \propto \sqrt{\frac{N_{transit}^2}{\sum_i N_i^2}} \propto \sqrt{\frac{1}{T}} \propto a^{-\frac{3}{4}}, \tag{F10}$$

which decreases with the increasing orbital period.

In summary, as short-period (nearly) circularized planetesimals usually start with small q_0 (tidal circularization timescale increases most rapidly with q_0), they tend to possess large transit probability and large SNR. The SNR generally decays towards an earlier stage of tidal evolution (larger a, T and e). On the other hand, as a population of planetesimals could be in a wide range of tidal evolution stages due to different tidal evolution time and tidal response, a planetesimal on a long-period highly eccentric orbit (early tidal evolution stage) does not necessarily have a low transit probability.

G The Roche limit of non-spherical objects

We consider two simple non-spherical bodies: an oblate spheroid and a prolate spheroid with semi-minor axis (short axis) to semi-major axis (long axis) ratio f. We further assume that the semi-minor axis of the non-spherical planetesimal is the spin axis, and that the mass and density of the non-spherical planetesimal is identical to its spherical counterpart.

Similar to the spherical case (Section 2.2 in the main text), the balance for an oblate spheroid can be expressed as (using the gravitational potential in Davidsson, 1999):

$$\frac{2GM_*a}{r_{Roche}^3} + \omega_p^2 a = GA_o(f)\rho_p a + \frac{\sigma_s \pi f a^2}{M_p}, \tag{G1}$$

where a is the semi-major axis of the planetesimal, $M_p = \frac{4}{3}\pi R_p^3 \rho_p = \frac{4}{3}\pi f a^3 \rho_p$, $A_o(f)$ is of the form:

$$A_o(f) = \frac{2\pi f}{(1-f^2)^{\frac{3}{2}}} \tan^{-1}\sqrt{\frac{1}{f^2}-1} - \frac{2\pi f^2}{1-f^2}. \tag{G2}$$

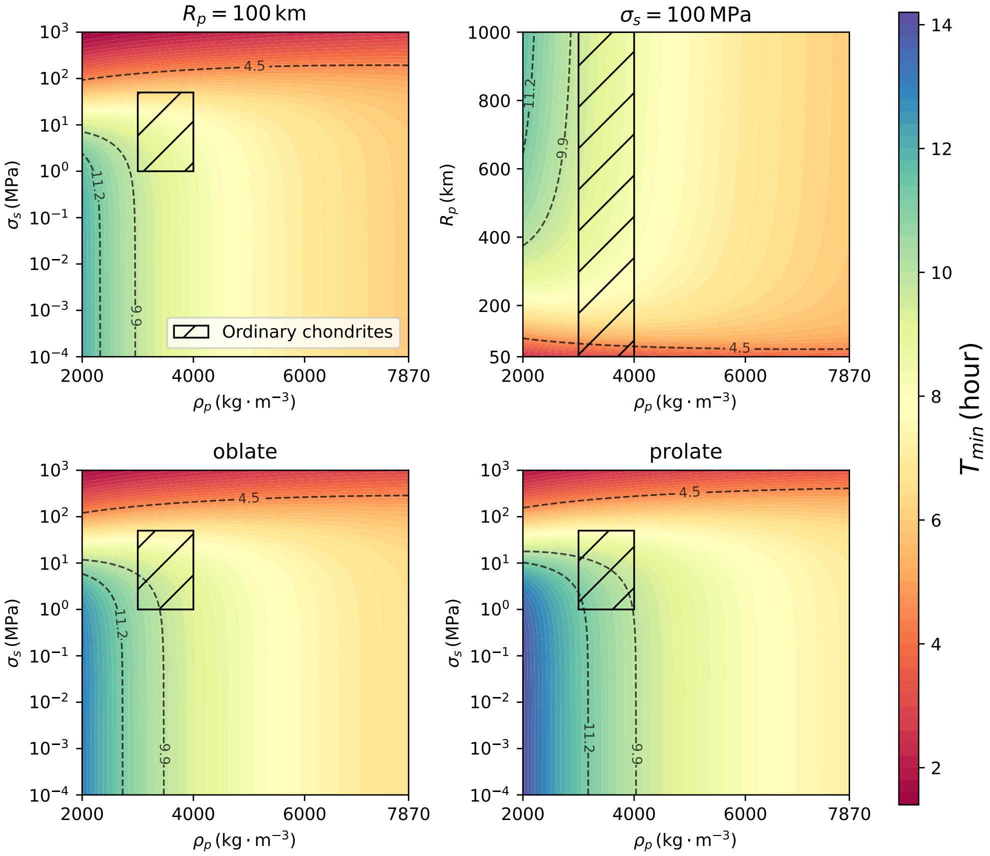

Figure G1: The minimum orbital period that a spherical planetesimal can circularize to without being tidally disrupted in ρ_p–σ_s space (upper-left panel) and ρ_p–R_p space (upper-right panel), together with its counterpart of an oblate spheroid (lower-left panel) and prolate spheroid (lower-right panel). Both spheroids have semi-minor axis to semi-major axis ratio $f = 0.7$. Other system properties are listed in Table 3 in the main text. The x-axes terminate at the density of iron the hatched rectangle represents the estimated property range of ordinary chondrites (H chondirtes, L chondrites, and LL chondirtes) (Pohl & Britt, 2020). The dashed lines correspond to the inferred periods seen in the optical transits of WD 1145+017 (4.5 hr) and ZTF J0328-1219 (11.2 hr and 9.9 hr) (Vanderburg et al., 2015; Vanderbosch et al., 2021).

The approximated Roche limit is hence:

$$r_{Roche,oblate} = \left[\frac{3.36125GM_*}{GA_o(f)\rho_p + \frac{3\sigma_s f^{\frac{2}{3}}}{4R_p^2\rho_p}}\right]^{\frac{1}{3}}, \tag{G3}$$

The balance for an prolate spheroid can be approximated as:

$$\frac{2GM_*a}{r_{Roche}^3} + \omega_p^2 a = GA_p(f)\rho_p a + \frac{\sigma_s \pi f^2 a^2}{M_p}, \tag{G4}$$

where $M_p = \frac{4}{3}\pi R_p^3\rho_p = \frac{4}{3}\pi f^2 a^3\rho_p$, $A_p(f)$ is of the form:

$$A_p(f) = \frac{2\pi f^2}{(1-f^2)^{\frac{3}{2}}}\ln\frac{1+\sqrt{1-f^2}}{1-\sqrt{1-f^2}} - \frac{4\pi f^2}{1-f^2}, \tag{G5}$$

The corresponding Roche limit can be approximated as:

$$r_{Roche,prolate} \approx \left[\frac{3.36125GM_*}{GA_p(f)\rho_p + \frac{3\sigma_s f^{\frac{4}{3}}}{4R_p^2\rho_p}}\right]^{\frac{1}{3}}, \tag{G6}$$

Alternatively, the Roche limit can be solved in the same way as Eq.11 in the main text.

For completeness, we also include the case where the semi-major axis of the prolate planetesimal is the spin axis;

$$\frac{2GM_*fa}{r_{Roche}^3} + \omega_p^2 fa = GA'_p(f)\rho_p fa + \frac{\sigma_s \pi f a^2}{M_p}, \tag{G7}$$

where $A'_p(f) = 2\pi - \frac{1}{2}A_p(f)$ and hence:

$$r_{Roche,prolate} \approx \left[\frac{3.36125GM_*}{GA'_p(f)\rho_p + \frac{3\sigma_s f^{-\frac{2}{3}}}{4R_p^2\rho_p}}\right]^{\frac{1}{3}}. \tag{G8}$$

In Fig.G1, we plot T_{min} reached at circularization. The upper-left panel is identical to Fig.10 in the main text. In the upper-right panel of Fig.G1, we plot T_{min} in ρ_p–R_p space at $\sigma_s = 100$ MPa. The effect of σ_s decays with the increase of R_p. Therefore, there may exist a scenario where the planetesimal undergoes partial tidal disruption and size contraction until the ultimate tensile strength is sufficient to support the body. In this case, the final size of the planetesimal on the ciruclarized orbit help constrain the ultimate tensile strength of the body.

In the lower panels of Fig.G1, we plot the analogues of the upper-left panel for an oblate spheroid (lower-left panel) and a prolate spheroid (lower-right panel) with semi-minor axis (short axis) to semi-major axis (long axis) ratio 0.7, and with the same density and mass as its spherical counterpart in the upper-left panel. We further assume that the semi-minor axis is the spin axis. When other conditions remain the same, a non-spherical planetesimal undergoes tidal disruption at a larger distance compared to its spherical counterpart, with the prolate planetesimal being the weakest against tidal disruption.

References

Barnes, J. W. 2007, PASP, 119, 986, doi: `10.1086/522039`

Beaugé, C., & Nesvorný, D. 2012, ApJ, 751, 119, doi: `10.1088/0004-637X/751/2/119`

Bolmont, E., Raymond, S. N., & Leconte, J. 2011, A&A, 535, A94, doi: `10.1051/0004-6361/201117734`

Burke, C. J. 2008, ApJ, 679, 1566, doi: `10.1086/587798`

Davidsson, B. J. R. 1999, Icarus, 142, 525, doi: `10.1006/icar.1999.6214`

Glanz, H., Rozner, M., Perets, H. B., & Grishin, E. 2022, ApJ, 931, 11, doi: `10.3847/1538-4357/ac6807`

Hansen, B. M. S. 2012, ApJ, 757, 6, doi: `10.1088/0004-637X/757/1/6`

Heller, R., Leconte, J., & Barnes, R. 2011, A&A, 528, A27, doi: `10.1051/0004-6361/201015809`

Hut, P. 1981, A&A, 99, 126

Leconte, J., Chabrier, G., Baraffe, I., & Levrard, B. 2010, A&A, 516, A64, doi: `10.1051/0004-6361/201014337`

Levrard, B., Correia, A. C. M., Chabrier, G., et al. 2007, A&A, 462, L5, doi: `10.1051/0004-6361:20066487`

Lu, T., Rein, H., Tamayo, D., et al. 2023, ApJ, 948, 41, doi: `10.3847/1538-4357/acc06d`

Matsumura, S., Peale, S. J., & Rasio, F. A. 2010, ApJ, 725, 1995, doi: `10.1088/0004-637X/725/2/1995`

Pohl, L., & Britt, D. T. 2020, Meteoritics & Planetary Science, 55, 962, doi: `https://doi.org/10.1111/maps.13449`

Rodet, L., & Lai, D. 2024, MNRAS, 527, 11664, doi: `10.1093/mnras/stad3905`

Rozner, M., Glanz, H., Perets, H. B., & Grishin, E. 2022, ApJ, 931, 10, doi: `10.3847/1538-4357/ac6808`

Tingley, B., & Sackett, P. D. 2005, ApJ, 627, 1011, doi: `10.1086/430494`

Vanderbosch, Z. P., Rappaport, S., Guidry, J. A., et al. 2021, ApJ, 917, 41, doi: `10.3847/1538-4357/ac0822`

Vanderburg, A., Johnson, J. A., Rappaport, S., et al. 2015, Nature, 526, 546, doi: `10.1038/nature15527`

von Braun, K., Kane, S. R., & Ciardi, D. R. 2009, ApJ, 702, 779, doi: `10.1088/0004-637X/702/1/779`